PCCP

Accepted Manuscript

ROYAL SOCIETY OF CHEMISTRY

www.rsc.org/pccp

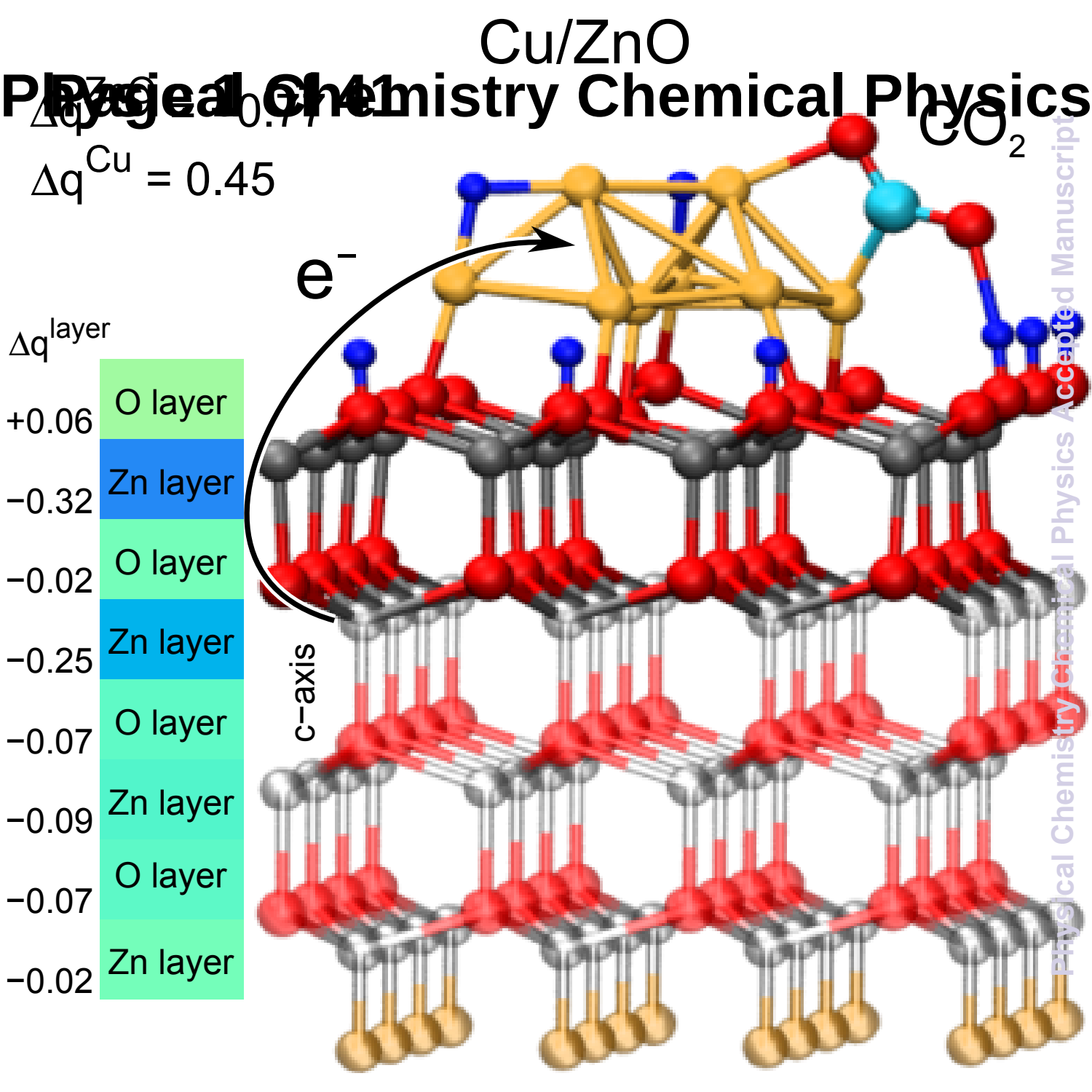

Cu/ZnO Nanocatalysts in Response to Environmental Conditions: Surface Morphology, Electronic Structure, Redox State and CO_2 Activation

Luis Martínez-Suárez, Johannes Frenzel,* and Dominik Marx

Lehrstuhl für Theoretische Chemie, Ruhr–Universität Bochum, 44780 Bochum, Germany

(Dated: October 10, 2014)

Abstract

Methanol synthesis is one of the landmarks of heterogeneous catalysis due to the great industrial significance of methanol as a clean liquid fuel and as a raw material for industry. Understanding in atomistic detail the properties of the underlying metal/oxide catalyst materials as a function of temperature and composition of the reactive gas phase is of utmost importance in order to eventually improve the production process. By performing extensive density functional theory based slab calculations in combination with a thermodynamic formalism we establish an atomistic understanding of gas phase-induced changes of surface morphology, redox properties and reactivity of ZnO supported Cu nanocatalysts. Extending our recent insights [PRL **110**, 086108 (2013)], we explore surface stabilization mechanisms and site-dependent redox states of both catalyst components as well as the pronounced electronic charge transfer processes across the metal-support interface. Moreover, *ab initio* molecular dynamics simulations unveil the vital role played by dynamical shape fluctuations of the deposited Cu_8 cluster. The pronounced structural flexibility of the metal nanoparticle is found to enhance CO_2 activation over Cu_8 at the elevated temperature conditions of the industrial methanol synthesis process, in addition to activation of CO_2 via electronic charge transfer from the ZnO support.

Keywords: oxide supported metal nanoparticles, strong metal–support interaction, surface thermodynamics, electron density of states, adsorbate structure, and ab initio molecular dynamics.

I. INTRODUCTION

Heterogeneous catalysis represents a vital prerequisite for industrial production of all types of substances and materials. It thus comes as no surprise that about 90% of all chemical manufacturing processes rely on this technology.[1] Development of more efficient catalysts, however, poses great challenges to scientific research. Pivotal to advances in catalyst materials design is a fundamental understanding of structure–activity relationships because modern heterogeneous catalyst systems typically consist of multi-component materials which develop their active morphologies only under reaction conditions.[1,2] Unique properties of nanoparticles not only arise in catalysis due to their size and structure, but also from their interactions with the supporting material.[3–8] Beyond the relevance to catalysis in the strict sense,[9] the general concept of "Strong Metal–Support Interactions" (SMSI) has been introduced[9,10] to describe structural and electronic properties which only arise from a synergistic combination of individual materials in direct contact, thus being not present in the separate materials.

One important example that brings these intricacies to light, in particular the SMSI effect, is the Cu/ZnO catalyst with Al_2O_3 serving as a stabilizer, which allows for efficient and highly selective synthesis of the very important bulk chemical methanol[11–13] in the so-called low-temperature "ICI process".[14] During the ICI process, methanol is mainly synthesized from CO_2 as the carbon source[15,16] by channeling a highly reactive syngas atmosphere (i.e. a mixture of H_2, CO and CO_2) over the catalyst while applying elevated temperatures and pressures of about 520 K and 5–10 MPa.[17] The catalyst itself typically consists of Cu nanoparticles (between 4 and 10 nm) separated by ZnO and the promoter material Al_2O_3.[18,19] Moreover, under these thermodynamic conditions the high concentrations of CO_2 and H_2 give rise to increased CO production via the reverse water-gas shift-reaction and decrease the selectivity of CO_2 over Cu/ZnO. Although both isolated components of the catalyst material, i.e. Cu and ZnO, are able to catalyze methanol synthesis themselves, there clearly exist synergistic effects between nanodispersed Cu and ZnO.[20–23] Presumably as a result of SMSI these effects lead to a much higher activity or to less drastic reaction conditions compared to, for instance, Cu surfaces[24,25], Cu clusters supported on other oxides,[26] or bare ZnO.[27] Note that a bare zinc oxide catalyst was industrially used in the well-known "BASF process", where CO is the carbon source.[28]

Several mechanistic reasons have been proposed to explain this improved catalytic activity of the combined system in terms of morphological changes of the catalyst surface,[27,29–31] which strongly depend on the environmental conditions applied.[32–35] It is now agreed that the particularly active morphology is generated under the elevated temperature and pressure conditions of the industrial process.[36,37] Moreover, it was shown that under conditions of methanol synthesis the overall activity of Cu/ZnO relates linearly to the specific Cu area.[23,27,38] In addition, fully reduced metal atoms with zero-valent redox state are present in methanol synthesis at atmospheric pressures,[26] while fixation of Cu in its monovalent oxidation state was shown to cause a decrease of the catalyst production rate.[23] Only very recently it was suggested that the active sites are located at the Cu^0/ZnO_x interface but no relation was found between the Cu^0 surface area and methanol synthesis rate using N_2O chemisorption.[39] Formerly, it had been proposed that the active site may consist of isolated cationic Cu atoms dispersed in the ZnO matrix, which itself should not be part of the active site but rather improve catalyst stability and Cu dispersion.[11] In contrast, more active roles of ZnO, which directly link to the reaction mechanism, have been proposed, e. g., the creation of Cu–Zn active sites[19,30,40] by alloying[31,33,36,41,42] or spillover of atomic H to Cu at low hydrogen partial pressures.[43,44] Furthermore, the specific reducible nature of the oxide substrate has been demonstrated[45] by separating the effects of structural and "synergistic" promotion, i. e., tuning of a preferential reaction path by tailored substrate materials. In addition, ZnO_x overlayers[19,26,46] were associated with a profound increase in the catalytic performance only recently,[45] while no Zn adspecies on Cu nanoparticles were found at reaction conditions[33,35] or could be associated with changes in the catalytic performance.[35] On the contrary, migration of reduced Zn atoms from the ZnO support to Cu was suggested to influence the morphology of the nanoparticles and to decrease the Cu surface area.[26] The existence of strain in the Cu/ZnO interface of the catalyst[27,36,37,47] was correlated with the methanol production rates[18,19,36] albeit other groups could not find a relation of microstructural strain and turnover frequency of methanol synthesis.[48] Ultimately, charge transfer effects taking place at the Cu/ZnO interface have been discussed to facilitate catalytic activity toward methanol synthesis from CO_2 being the source.[49] Indeed, in a recent study experimental evidence for strong electronic promotion via charge transfer from high-lying ZnO electronic states to the Cu Fermi level has been reported.[50]

Despite intense research, no consensus has been obtained yet on the active site or the

actual reaction mechanism of methanol synthesis over Cu/ZnO. The reasons for the often conflicting mechanisms proposed could be caused by the concurrent presence of multiple effects being at work and, therefore, giving rise to a myriad of catalyst morphologies in addition to the ones caused by SMSI.

More recently, however, significant progress has been made to disentangle reactivity and selectivity of Cu nanoparticles supported on different ZnO low-index faces. For instance, a synergy between Cu and ZnO was found to substantially improve selectivity of CO_2 activation and hydrogenation towards methanol production when the synthesis is conducted over metal nanoparticles supported on the polar surfaces of ZnO.[22] These faces are the predominantly active ones in methanol synthesis over the Cu-free, bare ZnO catalyst.[28,31,51,52] Being of Tasker-type-3, the ideal polar ZnO surfaces are fundamentally unstable due to an intrinsic dipole moment.[53] In this situation, the surface energy diverges toward infinity in the macroscopic limit and, therefore, polar surfaces cannot exist in nature without undergoing stabilizing electronic and/or morphological changes to achieve ideal charge neutrality.[53,54] In principle, there are three possible stabilization scenarios that quench the surface dipole moment to eventually reach ideal charge compensation: (I) The ionic charge on surface ions may be reduced to avoid "metallization of the polar surfaces" by partially filled O and Zn electronic bands;[54] (II) 1/4 of the surface ions may be removed from the surface, thus creating vacancies; (III) charged species may be adsorbed to reduce the oxidation state of the surface ions, e. g., H^+ and OH^-.[55] The interplay between all these possible stabilization mechanisms is intimately dependent on the thermodynamic conditions of the gas phase in contact with the polar ZnO surfaces.[54–56] The construction of thermodynamic surface structural phase diagrams revealed that the polar O–terminated ZnO$(000\bar{1})$ surface is covered by 1/2 monolayer (ML) of hydrogen within a wide range of oxygen and hydrogen partial pressures, which also includes catalytic conditions of methanol synthesis.[55] Recently, this was confirmed by extended phase diagrams which were based on larger surfaces slabs and moreover considered hexagonal and mulit-layer reconstructions in addition to adatoms on the ZnO$(000\bar{1})$ surface.[57,58] We note that at catalytic conditions of methanol synthesis the preferred stabilization mechanisms for the polar Zn-terminated ZnO(0001) is not ideal (as often used by ad hoc assumptions to study methanol plain ZnO or Cu/ZnO systems) or reconstructed but covered by 1/2 ML of OH.[56,59–61] After having established the basic stabilization properties, the reactivity of various bare ZnO surfaces was investigated by using a

sizable set of catalytically relevant probe molecules.[55,62–74] Subsequently, oxygen vacancies, i. e., various F centers, where identified as putative active sites on the ZnO($000\bar{1}$) surface acting as BASF catalyst material.[27,75,76] The dominating types and charge states of these defects were determined by the calculation of surface structural phase diagrams.[77] Furthermore, the calculation of the thermochemistry of methanol formation and oxidation on the defective ZnO($000\bar{1}$) surface revealed that several key species have a similar stability.[73,78] Thus, already at the level of the simple Cu–free ZnO catalyst, this leads to a highly interconnected reaction network as it is typical in heterogeneous catalysis. This complex network was successfully generated and explored by using advanced *ab initio* molecular dynamics sampling techniques.[79–81]

In the context of methanol synthesis on the more complex Cu/ZnO catalysts, the additional stabilization mechanisms due to the presence of Cu being a co-adsorbate must be considered as well[82–84]. Ultimately the strength of the adsorption of individual Cu atoms, monolayers and thin films has been shown to directly depend on the electronic structure of the particular oxide surface.[82] Ideal charge compensation and therefore structural stabilization of ZnO($000\bar{1}$) is achieved as soon as the surface bands are filled. At this point, the Cu–Cu cohesion energy dominates over the Cu−ZnO adhesion energy[82] and multi–layers or three–dimensional nanoparticles start to grow instead of two-dimensional deposition.[82,85–87] Based on this background and using well-tested methodologies we started to explore the structure and composition of nanodispersed Cu on ZnO.[88] In this recent letter, a model system consisting of a Cu_8 cluster deposited on the O–terminated ZnO($000\bar{1}$) surface in conjunction with DFT calculations was used to establish a preliminary thermodynamic surface phase diagram (see Fig. 2 for an extended version calculated within the present work) unveiling the relative energetics and the properties arising from SMSI in response to the redox properties of the gas phase. Depending on the chosen O and H chemical potentials of the gas phase we found that the interplay between ZnO surface stabilization and maximizing Cu cohesion energy within the nanoparticle determines distinct changes in surface morphology and oxidation state, and thus affects the overall reactivity of the catalyst. Under the H–rich environment of industrial methanol synthesis the ZnO surface is in a reduced state and the reactivity of the metal cluster towards CO_2 is enhanced by electronic charge transfer via the Cu/ZnO interface. In contrast, Cu−Zn surface alloying sets in only under severely reducing conditions while O vacancies, which are often discussed as pinning centers for supported

metal clusters,[89–91] are not stable given the compositions of the gas phase in the relevant pressure and temperature range.

In this paper, we provide detailed insights into the gas phase-induced changes of the morphology, electronic structure, and redox state of ZnO($000\bar{1}$) supported Cu nanoparticles depending on the thermodynamic conditions of the gas phase. The details of the methods, the Cu_8/ZnO($000\bar{1}$) model systems and the computational parameters are provided in Sec. II. Using this approach, we prepared and studied a large set of model systems consisting of eight Cu atoms interacting with an O-terminated polar ZnO slab in order to model the more complex industrial catalysts, which usually consist of much larger Cu particles being separated by smaller ZnO nanoparticles or supported on ZnO surfaces[92–95]. As a first step, we have performed DFT calculations in conjunction with an atomistic thermodynamics approach to extend our preliminary structural surface phase diagram.[88] In a second step, we performed an extensive electronic structure analysis of our Cu_8/ZnO($000\bar{1}$) nanocatalyst models to obtain a spatially resolved picture of local redox states of both the Cu nanoparticle and the ZnO($000\bar{1}$) surface with a focus on the industrially relevant phases as determined by temperature and pressure conditions. Having analyzed the catalyst models in such detail, in the third step we selected five distinctly different nanocatalyst structures and probed their reactivity toward activation of CO_2 which is the first step of industrial methanol synthesis relying on Cu/ZnO-based catalysts. We conclude with Sec. IV by summarizing our main results and putting them in a broader context.

II. COMPUTATIONAL METHODS

The ZnO slab structures were modeled using 4×4 lateral extended surface unit cells which are periodically repeated and consisted of four double layers of ZnO. The slabs were separated by a vacuum region with a thickness of $\approx 15\,\text{Å}$ in the crystallographic $\vec{c}$ direction (see Fig. 1). The copper clusters containing eight atoms were deposited on the polar oxygen-terminated ZnO($000\bar{1}$) surface. The different oxidation states of our catalyst models were adjusted by adding H atoms to the metal nanoparticles or to bare O atoms of the ZnO($000\bar{1}$) surfaces (see e.g. the 1/2–H–sym case depicted in Fig. 1), creation of O–vacancies by removing O atoms, alloying by adding a Zn atom to the cluster or overgrowing of the support by adding ZnO dimers on top of it, as well as combination of all these possibilities. In

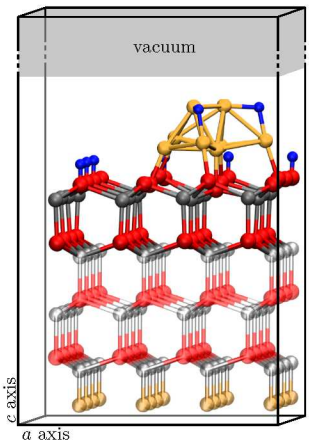

Figure 1. Schematic view of the 1/2 ML hydrogen saturated $Cu_8/ZnO(000\bar{1})$ slab model (1/2–H–sym). Zinc, oxygen, hydrogen and copper atoms are represented by grey, red, blue and golden spheres, respectively. Pale colors are used to indicate the frozen atoms of the bulk bottom layers of ZnO. Following Ref. 54, broken bonds at the Cu-free bottom face of the slab have been saturated by hydrogen-like pseudo-atoms shown in pale yellow.

order to distinguish the different configurations, we use the following labeling convention for the $Cu_8/ZnO(000\bar{1})$ catalyst models: x/y–H indicates the hydrogen coverage in monolayers, Zn–ad alloying of Zn into the Cu cluster, ZnO–ad overgrowing of support material onto the metal nanoparticle, O–vac the creation of a O vacancy, and a plus sign connects combinations of these basic patterns. By construction, bulk Zn–O bonds were broken at the bottom of the slab thus establishing a polar zinc-terminated ZnO(0001) which has been made charge neutral by hydrogen-like pseudo-atoms carrying a nuclear charge of +3/2 (see Ref. 54). In this way not only the charge density of bulk ZnO is enforced at the bottom layers, but also the dipole along the $\vec{c}$ direction is decreased to a residual minimum which has been carefully checked against an explicit dipole correction scheme[96]. In addition, the atomic positions of six layers, as being counted from the bottom of our slab model (highlighted using pale colors in Fig. 1), were kept frozen in structure optimizations and molecular dynamics simulations thus following our previous work. Note that this setup is similar to the one of Meyer and Marx when studying Cu adatoms and Cu layers on the very ZnO surface[82] and identical to the one which we have established recently.[88] Typically, a slab consisted of a total of 152 Zn, O and Cu atoms in addition to up to 13 atoms due to adsorbate species, i. e., H atoms, Zn–O dimers and CO_2 molecules. Given our final goal of performing extensive AIMD

simulations the size of our models is certainly at the edge of what is nowadays affordable with respect to accessible computer time. Nonetheless, we have demonstrated previously that Cu clusters consisting of eight atoms properly capture the cohesive properties while variations in shape and size of the cluster will affect the position of the phase boundaries only slightly.[88] Moreover, electronic charge distribution at the metal/oxide interface, being important for the activation of adsorbed reactant molecules, was demonstrated to be essentially independent of cluster size and shape for a closely related metal/oxide system, namely Au_n clusters with $n = 11, \ldots, 16$ on TiO_2.[97]

Static DFT calculations[98,99] and dynamic AIMD simulations[100] were carried out using the `Quantum Espresso`[98] and `CPMD`[99] program packages, respectively, employing the PBE generalized gradient approximation[101] (GGA) to account for the exchange–correlation contributions to the DFT total energy. Reference calculations using the Hubbard U approach[102] demonstrate the reliability of our results for the present Cu/ZnO model systems when used in conjunction with this semilocal functional, i. e.,PBE+U (see Sec. 7 of the Supporting Material). A plane wave basis was used to describe the wave functions of the valence electrons up to 25 Ry of kinetic energy. The zinc $3d$ semicore electrons were explicitly treated as valence states for all single-point electronic structure analyses such as calculations of band structures and local oxidation states. In order to reduce the computational cost at virtually no loss in accuracy, these states were included in the pseudopotential for the two Zn layers at the bottom of the slab in all structure optimizations and AIMD simulations. The interaction of core and valence electrons was represented by Vanderbilt ultra–soft pseudopotentials[103]. Converged values of total energies and other properties required an integration of the Brillouin zone employing a dense $4 \times 4 \times 1$ k–point mesh which was constructed following the algorithm of Monkhorst-Pack.[104] Γ–point only calculations were sufficient to relax the positions of the nuclei until the largest component of the residual forces was below 6 meV/Å. Having obtained the surface energies with an increased k-point sampling and using the same atomistic *ab initio* thermodynamics approach[55,105–109] as before, we calculated a refined and extended structural surface diagram compared to the preliminary one.[88] Short AIMD runs were carried out to determine structural stability of the surface structures up to temperatures of 800 K which are above the 600 K applied during industrial catalyst activation procedures but below the temperatures at which the catalyst undergoes major decomposition as seen in temperature programmed reduction experiments.[22] These simulations were carried out

within the canonical ensemble with temperature control by Nosè-Hoover chains[110] and thermostatting separately all degrees of freedom of the nuclei.

Starting from the self-consistent electronic density obtained with the $4\times4\times1$ k point grid we calculated the electronic band structure (BS) of the surface structures along the special k-path from Γ to M. This part of the Brillouin zone is found to cover the important features of the complete BSs. The electronic density of states (DOS) is calculated from the same self-consistent electronic density but for this purpose a $12\times12\times1$ Monkhorst-Pack mesh[104] was used for Brillouin zone integration. By expanding in terms of an atom-centered basis in conjunction with Löwdin population analysis[111] we obtained the projected DOS (pDOS); the states have been broadened using Gaussian functions of 0.05 eV width.

The thermodynamic stability of CO_2 molecules on the different $Cu_8/ZnO(000\bar{1})$ models is quantified by the adsorption energy, $E_{\mathrm{ads}}^{\mathrm{CO_2}}$, which is calculated as usual from

$$E_{\mathrm{ads}}^{\mathrm{CO_2}} = E_{\mathrm{CO_2@cat}}^{\mathrm{KS+vdW}} - (E_{\mathrm{CO_2}}^{\mathrm{KS+vdW}} + E_{\mathrm{cat}}^{\mathrm{KS+vdW}}) \,, \tag{1}$$

with $E^{\mathrm{KS+vdW}}$ corresponding to the Kohn–Sham total energies using the extended k-point sampling scheme plus energetic contributions from a dispersion correction[112] to account for van der Waals interactions. The latter might become important for describing adsorption and desorption processes on/from the catalyst surface via AIMD, which previously turned out to be key to the reaction mechanism of methanol synthesis over *bare* ZnO.[81] However, in view of our computational approach to heterogeneous catalysis employing AIMD[80] we are restricted to using parameterized semiempirical approaches due to their low computational demands. Nonetheless, these approaches were demonstrated to reasonably describe dispersion interactions of molecules on coinage metal surfaces if only the low-coordinated atoms of the metal surfaces are considered in evaluating the correction.[113,114] This naturally applies to our Cu_8 clusters given their small size and thus low-coordination numbers. Negative values of $E_{\mathrm{ads}}^{\mathrm{CO_2}}$ indicate thermodynamically stable adsorption.

In order to characterize the redistribution of electronic charge Δq^X between different parts X of two different surface structures (e. g., ZnO support, Cu cluster, and adatoms), we projected[111] the electronic charge density onto atom-centered electronic populations yielding partial charges $q_i, \forall i \in X$. For example the transfer from or onto the ZnO substrate (i.e.

$X = \mathrm{ZnO}$) is calculated following

$$\Delta q^{X=\mathrm{ZnO}} = \sum_{i \in \mathrm{O,Zn}} \left(q_i^{\mathrm{cat}} - q_i^{\mathrm{ref}} \right) , \tag{2}$$

where q_i^{cat} is the electronic population of atom i of the ZnO support of the catalyst model of interest and q_i^{ref} is that of the corresponding atom i of another of our calculated structures acting as reference. When analyzing bare catalyst Cu/ZnO surface structures the 3/8–H–flat model is used exclusively as reference, while in the case of CO_2 adsorption the latter is always represented by the isolated structures of molecular CO_2 and the corresponding free catalyst.

Thermodynamically most favorable adsorption sites of four $Cu_8/ZnO(000\bar{1})$ catalyst structures (i. e., 1/2–H–sym, 3/8–H–surf, and Zn–ad+1/4–H) have been determined by a hierarchical scheme for mapping the PES of adsorption of CO_2 while increasing the accuracy of the calculation. The starting points of this exploration procedure where the optimized structures of the bare catalyst and the CO_2 molecule. The CO_2 molecule is placed over the surface in three different orientational arrangements with respect to the surface plane, i. e., one perpendicular and two different parallel ones, and in each of these configurations the molecule is placed with the carbon atom down at the vertices of regular grids positioned at different heights over the catalyst surface. The same procedure was applied in regions around the Cu cluster itself using a distribution of points on half spheres around the cluster. In the first step and using these initial structures, optimizations were performed allowing only the oxygens of CO_2 to relax their position, which effectively would allow to activate CO_2 via bending of the linear molecule. Selecting all bent structures plus those near to the ZnO and Cu surface atoms, in a second step we refined the PES by full optimization of CO_2 molecules. Eventually, we used the results of both optimization steps to compile the final PESs of adsorption of CO_2 at the three catalyst surface structures 1/2–H–sym, 3/8–H–surf, and Zn–ad+1/4–H (see Fig. S1 in the Supplementary Material).

In the final step the structures corresponding to the most stable local minima were selected and subjected to full optimizations of the positions of the atomic nuclei of CO_2 and Cu/ZnO (except for the bottom layers of the slab that are kept frozen in our slab model as defined in Fig. 1). Furthermore, we calculated adsorption sites of CO_2 on two more $Cu_8/ZnO(000\bar{1})$ catalyst structures, 1/2–H–top and ZnO–ad+1/2–H–b. Instead of carrying out the full preliminary exploration procedure for these structures we assumed similar local

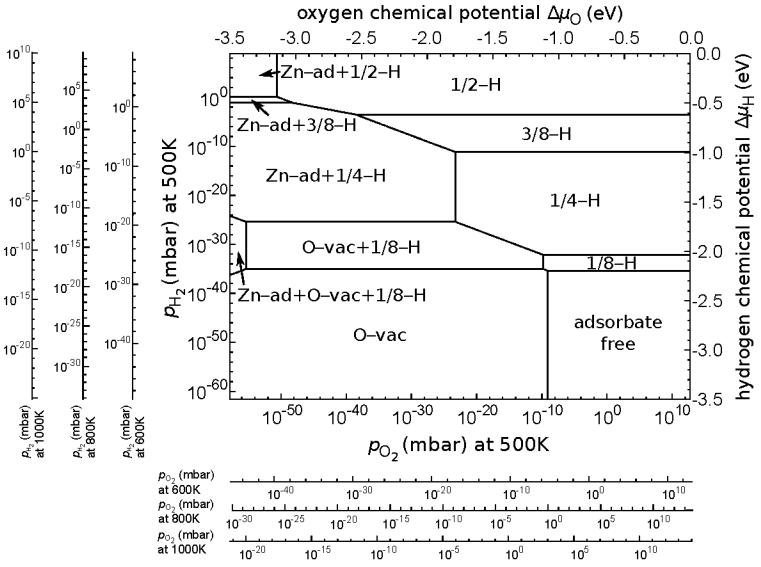

Figure 2. Extended structural phase diagram of the $Cu_8/ZnO(000\bar{1})$ supported nanocatalysts in thermodynamic equilibrium with H_2 and O_2 reservoirs controlling the chemical potentials $\Delta\mu_H$ and $\Delta\mu_O$. The corresponding partial pressures p_H and p_O are given for several temperatures including those roughly applied methanol synthesis conditions and at catalyst preparation, i. e., 500 K and 600 K; note that temperature programmed reduction has been carried out up to temperatures as high as about 1000 K.[22] In general, lower temperatures will favor H-rich and O-rich phases for given partial pressures and vice versa. Surface structures with the lowest free energies (see Supplemental Material for the complete data set) are labeled according to hydrogen coverage (x/y–H, in monolayers), zinc alloying into the copper cluster (Zn–ad), or oxygen vacancies (O–vac).

minima of adsorption of CO_2 compared to the PES of 1/2–H–sym, 3/8–H–surf, and Zn–ad+1/4–H that are used as initial structures for optimizations involving the 1/2–H–top and ZnO–ad+1/2–H–b models. A survey of the most stable adsorbate structures is summarized in Table S-4 to Table S-8 in the Supplementary Material.

III. RESULTS AND DISCUSSION

A. Redox properties and electronic structure of Cu/ZnO

In order to better understand the subtle interactions of oxide support and metal nanoparticle we determined the real-space structure, thermodynamic stability and electronic struc-

ture of in total 52 $Cu_8/ZnO(000\bar{1})$ structures.

These structures model possible surface chemical processes present in a wide range of oxygen and hydrogen partial pressures from the UHV regime up to the high pressure / temperature conditions of the industrial process of methanol synthesis which is carried out over the much larger nanostructures of the industrial catalyst. In particular, the processes of adsorption of H atoms on Cu atoms or O atoms on the support, migration of Zn atoms or ZnO dimers onto the metal cluster, creation of O vacancies and combinations of these processes were considered thus yielding 16 phases of $Cu_8/ZnO(000\bar{1})$: adsorbate–free, 1/8–H, 1/4–H, 3/8–H, 1/2–H, O–vac, O–vac+1/8–H, O–vac+1/4–H, O–vac+3/8–H, Zn–ad+1/8–H, Zn–ad+1/4–H, Zn–ad+3/8–H, ZnO–ad+1/8–H, ZnO–ad+1/4–H, ZnO–ad+1/2–H, Zn–ad+O–vac+1/8–H. In total, we have calculated the thermodynamic stability, surface structural phase diagrams for different temperatures (see Fig. 2) and electronic BS of 52 $Cu_8/ZnO(000\bar{1})$ structures. The complete set of data is gathered in Table S-1, Table S-2 and Table S-9 of the Supplemental Material.

The diagram in Fig. 3 visualizes the flow of presentation and, thus, may be used as a guide through the subsequent discussion of our results in various subsections. In particular, we focus only on those structures which have their phase stability in regions relevant to technological application, i. e., not only the reducing conditions applied to perform industrial methanol synthesis over Cu/ZnO but also conditions relevant to catalyst pre-treatment and re-reduction. In addition, fully oxidized phases will be discussed as they resemble potential product states in our AIMD approach that is able to disclose the entire reaction network for methanol synthesis from CO_2 over Cu/ZnO akin to *bare* ZnO.[79–81]

1. Fully oxidized bare ZnO(000$\bar{1}$)

In Fig. 4 the calculated BS and pDOS of seven selected Cu/ZnO structures are shown which is supplemented by the "ideal" Cu-free 1/2 ML hydrogen saturated $ZnO(000\bar{1})$ surface (1/2–H $ZnO(000\bar{1})$). Being exposed to elevated temperatures and pressures as well as reducing conditions of the surrounding gas phase applied in methanol synthesis, the 1/2 ML hydrogen coverage has been identified as the thermodynamically preferred surface termination of this polar O terminated face of $ZnO(000\bar{1})$.[54,55] Importantly, this 1/2 ML of H atoms ensures the filling of surface dangling bonds of this Tasker-type-3 unstable surface

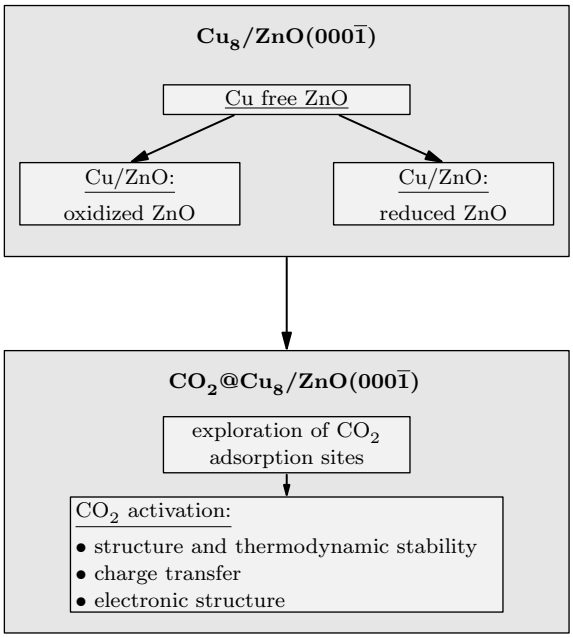

Figure 3. Flowchart visualizing the organization of presentation of the results.

and thereby provides charge neutrality and the characteristic band gap.[55] The additional electrons of the H adatoms fill up the only partially occupied surface state of ZnO($000\bar{1}$) which is reflected in the BS of 1/2–H ZnO($000\bar{1}$) (see Fig. 4(a)). The valence band (VB) builds up from O2p states, while Zn4s states and O2p states add mainly to the conduction band (CB) (indicated by the label B1 in Fig. 4(a)). Both are separated by a large band gap[115] being an indicator of a stable structure.

2. Cu/ZnO phases with fully oxidized support

The complexity of surface stabilization of the polar O terminated ZnO($000\bar{1}$) surface is found to be largely increased when, in addition, Cu is present in forms of adatoms, clusters or layers.[82,88] Filling of bands can now occur by 4s electrons of Cu which up to 1/2 ML leads to an overall increased binding energy of the adsorbate being similar to the one calculated for H adatoms at the same coverage.[82] In contrast to this regime, higher coverages of Cu are possible due to the cohesion energy in thin films or clusters, but the stabilization via the electronic mechanism of filling surface bands by Cu and H co-adsorbates will also add up if both species are present on the surface.[82] The situation becomes even more involved when we have to consider the surface coverage of these adspecies in a real system being governed by

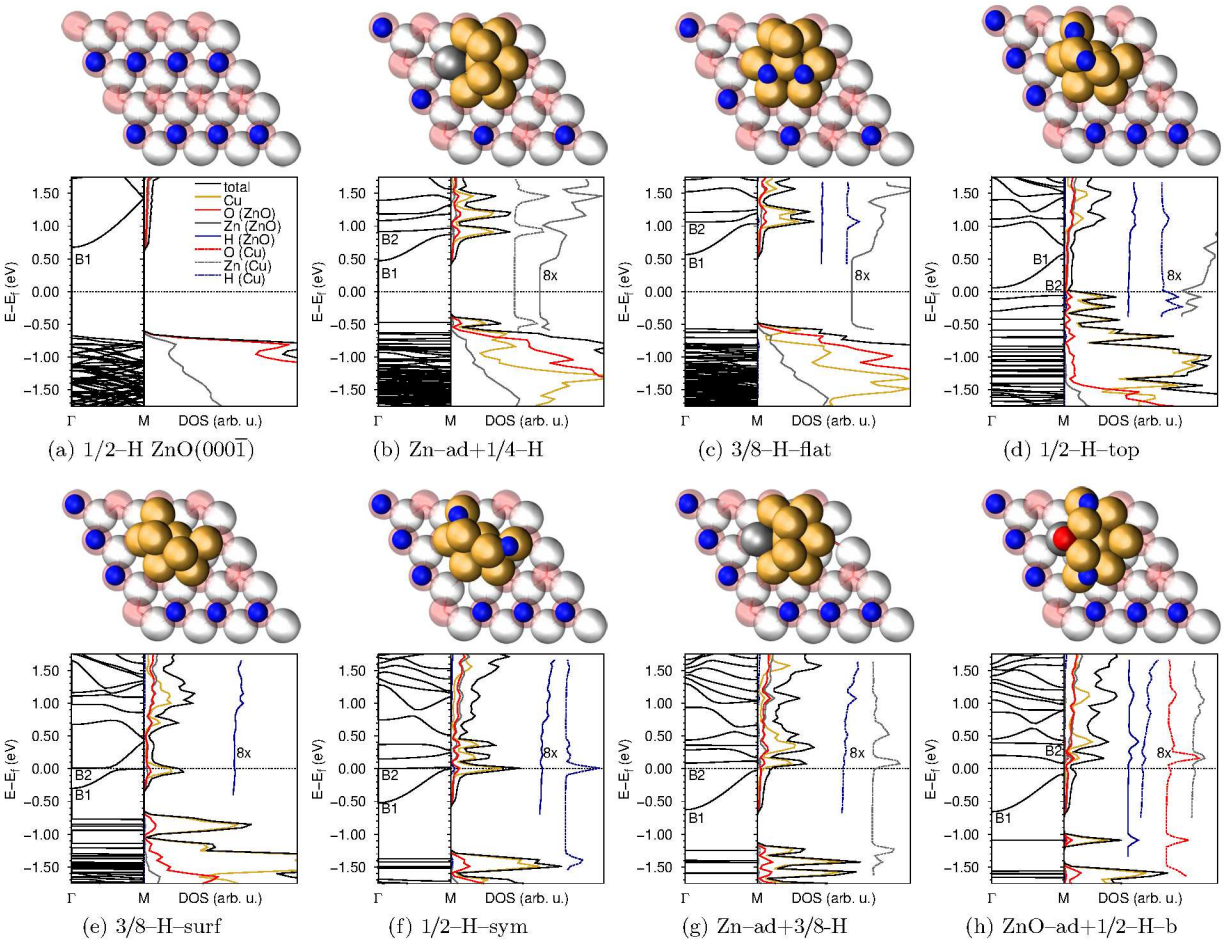

Figure 4. Real-space structure, electronic band structure (BS), and projected density of states (pDOS) of $Cu_8/ZnO(000\bar{1})$ surface structures: (a) ideal 1/2 ML hydrogen saturated oxygen terminated $ZnO(000\bar{1})$ surface (1/2–H $ZnO(000\bar{1})$) and the nanocatalyst models (b) Zn–ad+1/4–H, (c) 3/8–H–flat, (d) 1/2–H–top, (e) 3/8–H–surf, (f) 1/2–H–sym, (g) Zn-ad+3d8-H, and (h) ZnO-ad+1d2-H-b. Structures (b) through (d) and (g) are the lowest energy structures of particular phases of our surface phase diagram (see Fig. 2). The surface structure (top of the subfigure) shows oxygen, zinc, hydrogen and copper atoms by red, grey, blue and golden spheres, respectively. The labels B1 and B2 in the BS (bottom left part of subfigures) mark bands of ZnO and Cu character, respectively. In the same energy range close to the Fermi level the pDOS (bottom right part of subfigures) resolves atomic contributions stemming from the $Cu_8/ZnO(000\bar{1})$ nanocatalyst as well as adsorbate species on either the support or on copper are shown. Parts of subfigures (b), (e), and (f) were adopted from Ref. 88.

temperature, pressure and chemical composition of the surrounding gas phase. In particular, for Cu_8 nanocatalysts supported on ZnO there exists a subtle interplay of several stabilization mechanisms, i. e., H adsorption, O vacancies, adhesion of Cu, Zn-adatoms, as well as the gain of cohesion energy by formation of direct Cu-Cu and Zn-Cu interactions, which give rise to environmentally-induced changes in composition and morphology of the Cu catalyst.[88] This increased complexity allows for several phases of Cu/ZnO surface structures that share similar overall oxidation states of the ZnO support while at the same time these structures belong to different stability regions of the phase diagram (see Fig. 2). In the following we use this redox state of ZnO as a guide line to disentangle other properties of our supported nanocatalysts with the help of the calculated electronic structure.

a. Structure and phase stability. Here we start with $Cu_8/ZnO(000\bar{1})$ nanocatalyst structures with a fully oxidized support: Zn–ad+1/4–H, 3/8–H–flat, 1/4–H–b, and 1/2–H–a (see Fig. 4 and Supplemental Material for the latter two). According to the phase diagram of Fig. 2 the region of thermodynamic stability of these fully oxidized structures spans over a broad range of elevated chemical potentials $\Delta\mu_H$ of about $-2.0\,eV$ to $-0.5\,eV$. At low oxygen chemical potentials $\Delta\mu_O$ below $-2.\,eV$ Zn–ad+1/4–H is preferred while the pure H stabilized phases occur at higher $\Delta\mu_O$. Herein, Zn–ad+1/4–H, 3/8–H–flat, and 1/4–H–b are the local minimum structures within their phase, while 1/2–H–a is less stable compared to the thermodynamic minimum 1/2–H–top of the 1/2–H phase (see Fig. 4d). The energy difference of these two is only 0.1 eV and, therefore, we suspect 1/2–H–a to represent a possible transition between 3/8–H–flat and 1/2–H–top phases. Furthermore, the calculated phase diagram of Fig. 2 can explain the temperature dependence of the stability of the different catalyst/surface structures. At high temperatures of about 800 to 1000 K, which are typically applied during catalyst preparation and re-activation processes, the Zn–ad+1/4–H phase will become thermodynamically accessible also at somewhat higher partial pressures of O and H compared to the lower temperatures. In contrast, H-rich and O-rich phases are preferred at thermodynamic conditions of the methanol synthesis itself over Cu/ZnO, i. e., at about 500 K and partial pressures p_H from about 10^3 to 10^6 mbar and p_O from ca. 10^{-12} to 10^{-6} mbar the phase stability region has shifted even deeper into the 1/2–H phase and, thus, further away from 3/8–H and Zn–ad+1/4–H phases.

b. Electronic structure. In order to understand the broad phase stability region of phases with oxidized support we will now analyse their structures and electronic structure

relationship in detail. All four fully oxidized structures share one common stabilization pattern of the O-terminated ZnO(000$\overline{1}$) surface, i. e., hydroxylation of O atoms of the support by 1/4 ML of H atoms; note that our structure labels encode the coverage of the catalyst by H atoms in ML units thus including substrate *and* metal. This fixed concentration delivers half of the electrons needed to fill the surface bands of ZnO(000$\overline{1}$) and, as such, H atoms are the basis for surfaces stabilization in this broad range of $\Delta\mu_{\mathrm{H}}$ values. In order to achieve full surface oxidation the metal cluster must contribute the remaining electrons which in terms of this simple electron counting scheme would require 1/4 ML of Cu bound to surface O atoms, *vide supra*. Comparing the surface structures and calculated BS this threshold is exceeded in all four structures as Cu realizes at least a 3/8 ML, i. e., six to seven Cu−O bonds. In the calculated BS and pDOS of all four structures (see Fig. 4b and Fig. 4c, as well as Table S-9p Table S-9h of the Supplemental Material) we find the O-2p band of ZnO to be fully occupied. In addition, the characteristics of the CB, which for this supported nanoparticle system is the surface Zn band, is similar to the BS known from the Cu-free 1/2–H–ZnO(000$\overline{1}$) surface (see Fig. 4a), and this is what we obtained for Zn–ad+1/4–H, 3/8–H–flat, and 1/2–H–a. Although several Cu states range into the bottom of the gap of the bands of ZnO and the VB is a localized state of mainly $\mathrm{Cu_s}$, these three structures exhibit a relatively wide band gap which is smaller compared to the one of 1/2–H–ZnO(000$\overline{1}$). The fourth fully oxidized surface structure, 1/4–H, is exceptional. With no adatoms on Cu the BS of 1/4–H–b (see Table S-9h) has a much smaller band gap. Both VB and CB are localized at the Cu nanocluster, while the separation of ZnO surface bands is largely unaffected. Clearly, the pDOS of 1/4–H–b shows a CB being a Cu state, which has been emptied compared to the other three models and, thus, indicates oxidation of the metal cluster. When now focusing more on regions of higher μ_{H} or lower μ_{O} values within the phase stability of the fully oxidized Cu/ZnO surface structures, empty metal states can be filled by electrons from H and Zn adatoms on Cu, i. e., 3/8–H–flat and 1/2–H–a, and Zn–ad+1/4–H, respectively.

c. Electronic charge transfer. Besides the redox properties of a bare metal cluster the concentration of H adatoms on Cu seems to mediate its adhesion to the ZnO substrate, i. e., 3/8–H–flat and 1/2–H–a). In contrast, cohesion energy is gained in the creation of Cu−Cu and Zn−Cu interactions in the absence of this type of adatoms, i. e., 1/4–H–b and Zn–ad+1/4–H, respectively. Moreover, electronic charge transfer through the ZnO/Cu interface directly influences the overall oxidation state of substrate and metal particle and,

therefore, determine mechanisms of surface stabilization and methanol synthesis.[49,50,88] To gain further insights into these bi-directional charge transfer effects between metal cluster and oxide support and the environmentally-driven interaction with adspecies, we switch to a more convenient representation of the electronic structure data. Upon integrating the pDOS of the occupied states we obtain a projection of the electronic density to atom-centered populations q_i that allow for insights into charge redistribution effects Δq^X (see Eq. (2)) between distinct parts X of the supported nanocatalyst surface structures.

Using 3/8–H–flat as reference in Fig. 5 we have plotted Δq^X for the $Cu_8/ZnO(000\overline{1})$ structures of Fig. 4 and its structural parts, i. e., the Cu_8 metal cluster ($\Delta q^{\text{tot Cu}}$) and the complete ZnO support ($\Delta q^{\text{tot ZnO}}$), which is further resolved in terms of distinct layers of O and Zn atoms (Δq^{layer}) as well as individual atoms of the top-most surface layer (O layer).

We start the discussion with the comparison of Zn–ad+1/4–H and 3/8–H–flat (see Fig. 5a) which displays the redistribution of electronic charge upon changing the environment of the catalyst from O poor to O rich conditions, i. e., in our model we have to exchange a Zn adatom by two H adatoms, respectively. Being incorporated into the metal at the Cu/ZnO interface the Zn adatom leads to an increase of electronic charge of the ZnO substrate as well as the Cu cluster, with $\Delta q^{\text{tot ZnO}}$ of $0.34\,|e^-|$ and $\Delta q^{\text{tot Cu}}$ of $0.75\,|e^-|$, respectively. Similarly, recent high-pressure CO adsorption experiments point to a strongly reduced state of Zn-containing ZnO supported Cu catalysts as monitored by *in situ* spectroscopy.[116] Accordingly, analysis of Δq^{O} of Zn–ad+1/4–H resolves that the larger part of the excess charge is localized in the $Zn_{ad}-O$ bond to one O atom of the first O layer of $ZnO(000\overline{1})$. Providing all of the excess charge, the Zn-adatom at the Cu/ZnO interface itself becomes more positive, i. e., the absolute electronic charge of the Zn adatom is only slightly less than that of Zn atoms of bulk ZnO.

In stark contrast, in 3/8–H–flat the two H adatoms on Cu are charge neutral and, therefore, might affect the oxidation state of ZnO only marginally (see Fig. 5b) comparing 3/8–H–flat to 1/4–H–b). Maintaining the full oxidation state of the ZnO support in 1/4–H–b, the Cu cluster must contribute own charge density and therefore undergoes a mild oxidation compared to 3/8–H–flat and, therefore, is able to compensate the loss of electronic charge by forming additional Cu−Cu contacts as well as de-wetting of ZnO which, however, leads to the overall destabilization and emptying of Cu states, *vide supra*. Along these lines, even an increase of H adatom concentration on Cu, e. g., model 1/2–H–a (see Table S-1w of the

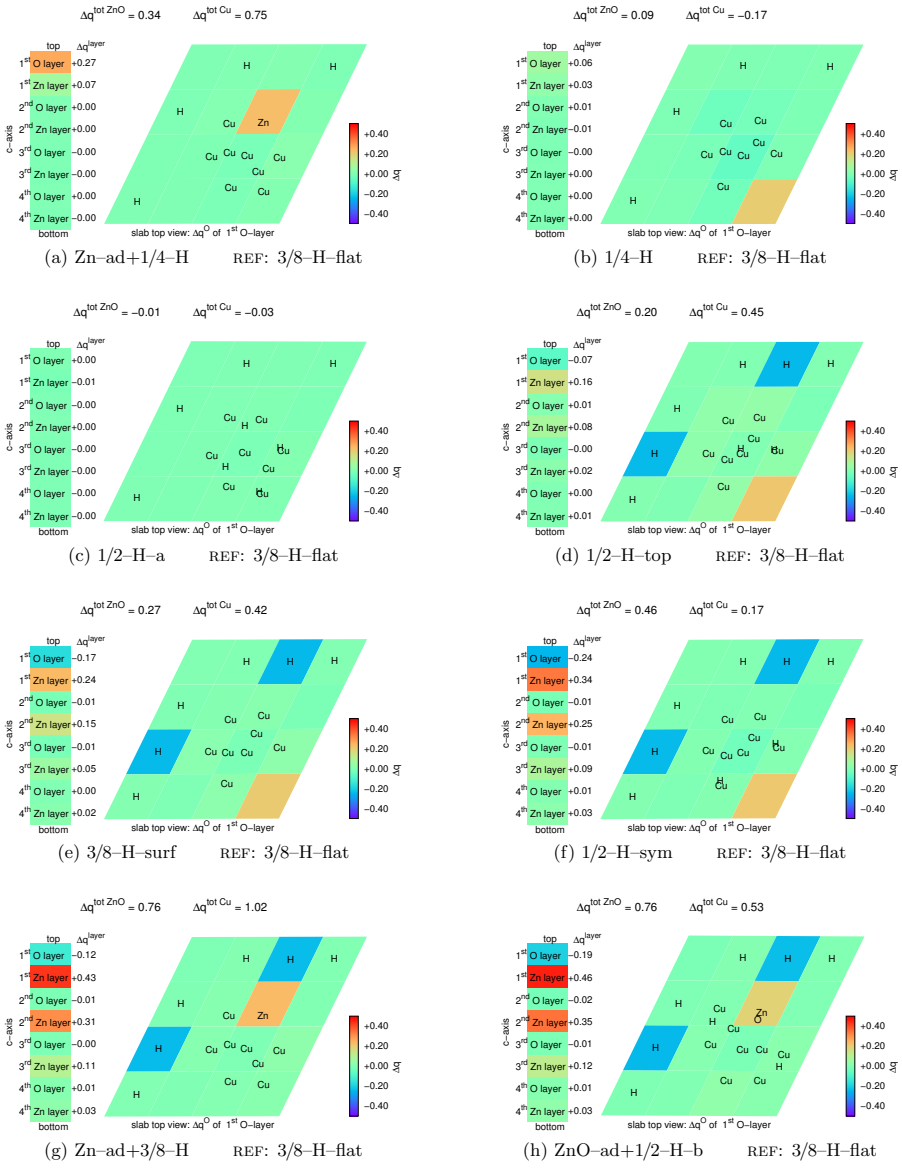

Figure 5. Change of the oxidation state of ZnO support and Cu nanocatalyst. The difference of the electron population of individual atoms, Δq^{X} , between two Cu/ZnO surface structure is depicted (see Eq. (2)). In all subfigures the same reference structure, 3/8–H–flat, is used. The spatial resolution of Δq is provided for the ZnO substrate and the Cu_8 nanocatalyst by $\Delta q^{\text{tot ZnO}}$ and $\Delta q^{\text{tot Cu}}$, respectively. Moreover, $\Delta q^{\text{tot ZnO}}$ is resolved down to the individual layers of the surface, i. e., the slabs of O atoms and Zn atoms, i.e. Δq^{layer} and Δq^{layer}, respectively, as well as to the O atoms of the surface O layer, i.e. $\Delta q^{\text{O atom}}$ (bottom right of the subfigures). Positive values of Δq (color code: yellow to red) indicate electron accumulation (corresponding chemically to reduction) compared to the reference, while negative values of Δq (color code: cyan to blue) indicate electron depletion (oxidation). The position of atoms of the catalyst structures which are above the O surface layer are indicated by their atom symbols; the atoms of the reference structure are not shown.

Supplemental Material) does not influence the oxidation state of the substrate (see Fig. 5c).

Finally, we will briefly discuss the change of oxidation state when shifting from high to low μ_O value while keeping the window of μ_H rather small with values between $-1.7\,eV$ and $-1.0\,eV$, i. e., changing from 1/4–H to Zn–ad+1/4–H phases according to our phase diagram (see Fig. 2). Under these extreme reducing conditions, which are the environmental conditions in industrial Cu/ZnO catalyst pretreatments, the presence of a Zn adatom on Cu leads to an electron-rich metal cluster in Zn–ad+1/4–H (see charge density difference plot Fig. S8c of the Supplemental Material). Very similarly, such Zn migration from ZnO has been observed experimentally for larger Cu clusters.[29,31,33,36,41] These surface science studies have been carried out under UHV conditions. Interestingly, the very pressure range falls into the phase stability region of the Zn–ad+1/4–H phase thus demonstrating that our rather small nanocatalyst structures describe these effects rather well. In contrast, Zn/Cu surface alloys have recently been suggested to act as active sites in methanol synthesis,[19] which would contradict our calculated phase diagram. However, *in situ* X–ray absorption fine structure spectroscopy finds the peculiar structure of the nanocatalysts to be maintained under process conditions,[33] thus supporting our theoretical findings. This was, in addition, confirmed by a most recent *in situ* neutron diffraction study showing alloy formation setting in only at temperatures much higher than those applied in industrial methanol synthesis.[35]

Given the fully oxidized nanocatalyst, i. e., 1/4 ML of H atoms on the substrate, our results of the charge redistribution suggest the following stabilization mechanisms between $ZnO(000\bar{1})$ surface and Cu_8 cluster: At O poor conditions excess charge of a Zn adatom allows to form additional Zn−Cu and Cu−Cu contacts leading to an overall gain in cohesion energy and partial reduction of the metal cluster. When changing to O rich conditions, i. e., into the phase stability of 3/8–H–flat, flatter metal clusters with H adatoms are preferred. Because the Cu_8 cluster of 3/8–H–flat must contribute more electronic charge to fill the ZnO surface band, the Cu-Cu cohesion energy is decreased compared to the one of Zn–ad+1/4–H. The H adatoms on the metal maintain their neutral charge.

3. Phases with reduced ZnO support

a. Structure and phase stability. High μ_H values above roughly $-0.6\,eV$ favor Cu/ZnO surface phases with an increased coverage of at least 3/8 ML of H atoms on the polar

O–terminated ZnO(000$\bar{1}$) support surface. This degree of hydroxylation of O atoms in addition to electronic charge donated by the Cu cluster guarantees the complete filling of ZnO(000$\bar{1}$) surface bands of our catalyst structures. More importantly, excess electrons are available which can either lead to reduction of oxide support or metal cluster, or both. In the surface phase diagram (see Fig. 2) emerge two distinct groups of "reduced" phases depending on whether the Cu cluster was subjected to Zn incorporation or not. The corresponding structural patterns are similar to the fully oxidized surface structures being discussed for oxidized supports, *vide supra*. Herein, extremely reducing, oxygen poor conditions with μ_O values below $-3.0\,\mathrm{eV}$ favor Zn–ad+3/8–H and Zn–ad+1/2–H phases, while 3/8–H and 1/2–H phases are largely stable in the broad range of μ_O above $-3.0\,\mathrm{eV}$. According to the surface phase diagram from Fig. 2, 1/2–H–sym is clearly the thermodynamically favored phase at those temperatures and pressures that are typically applied to synthesize methanol over Cu/ZnO, i. e., about 500 K and pressures ranges of 10^3 to 10^6 mbar for p_H and for p_O of 10^{-12} to 10^{-6} mbar. At these pressures but higher temperatures of 1000 K, the phase stability shifts toward 3/8–H and Zn–ad+1/4–H phases, while the extremely reduced Zn–ad+3/8–H and Zn–ad+1/2–H phases remain inaccessible at these conditions.

b. Electronic structure and charge transfer: 1/2–H phases. Starting our discussion with the 1/2–H phase, we obtained 1/2–H–top as the thermodynamically most stable surface structure with 1/8 ML of H adatoms being located on the Cu cluster. Fig. 4d shows that one H atom is adsorbed close to the Cu/ZnO interface while a second one bridges two Cu atoms at the top of the metal cluster. This distinct arrangement of the adatoms in conjunction with the higher degree of hydroxylation of ZnO(000$\bar{1}$), i. e., excess electronic charge, gives rise to a complex electronic structure at the Fermi level which is depicted in Fig. 4d. First of all, the BS of 1/2–H–top is characterized by a very small band gap. Additional localized electronic states of Cu fill the energy gap between ZnO surface bands ranging from $-1.5\,\mathrm{eV}$ to $-0.3\,\mathrm{eV}$. Secondly, VB and CB (labeled B2 and B1) share contributions from either states of metal cluster or bands of the oxide support. The reduction of 1/2–H–top mainly takes place at the metal cluster while the ZnO(000$\bar{1}$) surfaces receives a minor part of the excess charge (see Fig. 5d). Cu atoms are neutral or, if in contact with more than five other metal atoms, can be slightly reduced. The H adatoms on the metal cluster have atomic character. More importantly, a reduction of Zn atoms of the substrate takes places in 1/2–H–top which affects all layers of Zn, but predominantly the two closest to the surface. In particular, this

reduction changes the nature of the VB that becomes delocalized over Zn4*s* states of mainly the oxide surface, but also of the bulk part of the support.

An even more reduced ZnO(000$\bar{1}$) substrate is realized by 1/2–H–sym which energetically is about 0.5 eV less favorable compared to 1/2–H–top. The phase 1/2–H–sym solely differs in the position of the H adatoms on Cu both being bound to atoms at the metal/support interface (see Fig. 4f). This slight change in the position of H adatoms initiates a *fundamental* change in the electronic structure compared to 1/2–H–top! In the BS of 1/2–H–sym (see Fig. 4f) the ZnO(000$\bar{1}$) surface band B1 is completely filled while band B2 remains empty, i. e., corresponding to VB and CB, respectively. Moreover, in the energy gap between the states of the ZnO surface from -1.5 eV to -0.5 eV only some localized Cu states appear indicating an oxidation of the metal cluster. Taken together, the slight structural change between 1/2–H–top and 1/2–H–sym induces a spatial inversion of the electronic charge density between metal and support, i. e., $q^{\text{tot ZnO}}$ of 0.46 $|e^-|$ and $\Delta q^{\text{tot Cu}}$ of 0.17 $|e^-|$, (see Fig. 5f). Interestingly, the neutral character of the H adatom is maintained in 1/2–H–sym while the individual Cu atoms become slightly oxidized with respect to 1/2–H–top. The value of $q^{\text{Zn layers}}$ increases to 0.71 $|e^-|$ with the largest contribution going into the two topmost layers of Zn but distributing in the bulk layers, too. This reduction of the substrate does not change the oxidation state of O atoms at the Cu/ZnO interface, whereas this important part of the catalyst is slightly reduced within the 1/2–H–top structure.

c. Electronic structure and charge transfer of 3/8*–H phases.* Understanding the pronounced charge transfer between metal and support we investigated the 3/8–H–surf surface structure which has no H adatoms at the cluster but 3/8 ML H at ZnO(000$\bar{1}$). Belonging to the 3/8–H phase this nanocatalyst structure is only 0.2 eV less stable compared to the minimum 3/8–H–flat. Analyzing the electronic structure and electronic charge density (see Fig. 4e and Fig. 5e, respectively) one can see that 3/8–H–surf might represents a transition between 3/8–H–flat and 1/2–H–sym. The electronic properties of 3/8–H–surf nicely demonstrate that the transition to a reduced ZnO(000$\bar{1}$) surface starts with 3/8 ML of surface hydroxylation and an adatom-free Cu cluster. Herein, hydroxylation is the dominant factor, which provides additional electrons to the system, while H adatoms on the Cu cluster stay neutral and may have only modulating effects on the shape of the metal cluster rather than affecting the general oxidation state of either metal or substrate. If H atoms saturate dangling bonds of low coordinated metal atoms of the Cu/ZnO interface, 1/2–H–sym, the

nanoparticle becomes stabilized. More importantly, in such setup excess charge is able to reduce the ZnO($000\bar{1}$) substrate by filling bands located at Zn atoms of both, surface and bulk. In strong contrast, structure 1/2–H–top indicates that a low concentration of H adatoms on Cu at the metal/support interfaces is insufficient to maintain a reduced substrate. Instead, the excess charge is transferred over the boundary and onto the metal stabilizing its dangling bonds, eventually. However, we expect these effects to be less pronounced in larger clusters because the ratio of interface to surface Cu atoms will be also smaller.

d. Electronic structure and charge transfer: Zn–ad phases. Similar to the phases with fully oxidized ZnO substrate the incorporation of Zn adatoms into the Cu cluster will favor its reduction, but requires highly reducing conditions shifting μ_{H} to even more elevated values. Our phase diagram (see Fig. 2) shows two phases: Zn–ad+3/8–H and Zn–ad+1/2–H. Nonetheless, covering the essential features we will only discuss the first one. In the BS of Zn–ad+3/8–H (see Fig. 4g), band B1 belonging to the ZnO($000\bar{1}$) surface is fully occupied and energetically stabilized compared to 1/2–H–sym whereas the Cu state B2 stays empty. The additional charge of the Zn atom, which herein has the same cationic character as Zn–ad+1/4–H, is distributed over the metal cluster as well the O and Zn surface layers of the support (see Fig. 5g). Hereby, receiving the major part of the electrons, Cu atoms are charge neutral or even slightly reduced if highly coordinated, such as the central atom of the cluster.

e. Structures of ZnO-ad and O–vac phases. Finalizing this section, we will briefly summarize our results of selected Cu/ZnO catalyst structures which feature a reduced oxide substrate, but do not appear in our calculated phase diagram. In several cases these surface morphologies are thermodynamically less stable by some tenths of an eV and therefore might be (locally) relevant at larger sizes of Cu nanoparticles. Stimulated by recent experimental insights, we have investigated the SMSI effect of over-grown support material onto the Cu cluster[19], which is modeled by a ZnO dimer located at the metal/support interface. Varying the concentration of H atoms from 1/8 ML to 1/2 ML (see Fig. 4h and Table S-1W through Table S-1Z of the Supplemental Material) we find the ionicity on the ZnO dimer resembling that of the bulk material leading to strong O−Cu bonds. The BS and in particular the filling of ZnO surface band follows largely the electronic structure of Zn–ad structures given the same concentration of H atoms (see Table S-9P through Table S-9S of the Supplemental Material). The additional O adatom of the ZnO dimer in all cases leads to a considerable

oxidation of the metal cluster with respect to Zn–ad structures, e. g., see Fig. S10 in the Supplemental Material showing the charge density difference between ZnO–ad+1/4–H and Zn–ad+1/4–H surface structures. Moreover, our calculations did not yield ZnO–adspecies with Zn in a less oxidized state compared to ZnO bulk. Only very recently the stabilization of such an intermediate state of Zn (in terms of ZnO thin films on brass surfaces) was proposed to be the only role played by ZnO in industrial catalysts.[117] Secondly, high H concentration on the substrate reduce the ZnO surface in the presence of Zn adatom and ZnO addimers on the Cu cluster (see Fig. 5g and Fig. 5h, respectively). Thirdly, the effect of O vacancy creation was investigated, which represents an alternative surface stabilization mechanism to hydroxylation of ZnO($000\bar{1}$) itself.[77,82] Substituting two H atoms, one vacancy accounts for the same number of electrons in filling surface states but also causes a defect state to appear in the band gap.[55,77] This is supported by the electronic structures of catalyst models O–vac+1/4–H and O–vac+3/8–H (see Table S-1H and Table S-9A, and Table S-1I and Table S-9B in the Supplemental Material, respectively), which, accordingly, feature a very similar BS compared to that of 3/8–H–surf and 1/2–H–sym. Moreover, the charge density difference plots of Table S-2g and Table S-2h demonstrate that the O vacancies have a local impact on the electronic structures only. The oxidation states of the bulk part of the oxide substrate and Cu cluster hardly changes while the additional electronic charge is accumulated at the Zn atoms of the vacancy. Similar redox state dependent charge localization at such F–centers have been studied in our recent series of investigations addressing methanol synthesis over Cu-free ZnO($000\bar{1}$) surfaces, thus demonstrating the role of such O vacancies as potential active sites.[77–80]

B. Structural and electronic properties of CO_2 on Cu/ZnO nanocatalysts

After having obtained comprehensive insights into the redox properties of the Cu/ZnO system we now focus on its chemical reactivity. The initial step in the heterogeneous catalytic process of methanol synthesis over the ICI catalyst is the activation of CO_2 which is the main source of carbon.[15,16] To classify such an activation of CO_2 on the catalyst surface, C−O bond length, O−C−O bond angle, and atomic charges are commonly used as indicators in comparison to the linear configuration in the gas phase.[118] Alternatively, the activation of molecular CO_2 in the presence of charge transfer from the catalyst can be explained based on

Table I. Structural, electronic and thermodynamic characteristics of activated CO_2 on Cu/ZnO; note that all underlying structures have been fully optimized within our slab model. Adsorption energies of CO_2 E_{ads} (for the full list see Table S-8 of the Supplemental Material), C−O bond lengths d_{C-O}, bond angle $\angle_{O-C-O}$ of the adsorbed molecule and differences of the electronic population of specific atoms Δq (see Eq. (2)), i. e., $\Delta q_{CO_2}(C)$ and $\Delta q_{CO_2}(O)$ of the C and O atoms of CO_2 were calculated w.r.t. an isolated CO_2 as reference, while Δq_{Cu}, Δq_{ZnO} and Δq_{Zn-ad} are the charge difference of CO_2@Cu/ZnO and CO_2–free Cu/ZnO for the sum of all Cu atoms, the sum of all Zn and O atoms of the ZnO support, as well as Zn and O adatom on the cluster, respectively. Positive values of Δq correspond to electronic charge accumulation (i.e. chemical reduction) compared to the CO_2-free surface.

Catalyst model	CO_2 ads.site	E_{ads} (eV)	d_{C-O} (Å)	$\angle_{O-C-O}(^\circ)$	$\Delta q_{CO_2}(C)$	$\Delta q_{CO_2}(O)$	Δq_{Cu}	Δq_{ZnO}	Δq_{Zn-ad}
1/2–H–sym	O (Fig. 6h)	−0.82	1.26, 1.29	127.3	0.10	0.29	−0.06	−0.14	
3/8–H–surf	O (Fig. 6g)	−0.85	1.27, 1.28	127.6	0.09	0.27	−0.21	−0.01	
1/2–H–top	O (Fig. 6f)	−0.83	1.25, 1.28	129.5	0.10	0.29	−0.18	−0.05	
Zn–ad+1/4–H	O (Fig. 6e)	−1.09	1.26, 1.27	128.8	0.09	0.35	−0.04	−0.28	0.04
ZnO–ad+1/2–H–b	O (Table S-7d)	−0.96	1.24, 1.28	129.4	0.08	0.54	−0.16	−0.26	0.04
1/2–H–sym	Cu (Fig. 6d)	−1.41	1.31, 1.30	122.8	0.35	0.17	0.45	−0.77	
1/2–H–sym-b	Cu (Table S-3b)	−1.28	1.26, 1.28	130.6	0.30	0.20	0.12	−0.39	
3/8–H–surf	Cu (Fig. 6c)	−1.11	1.23, 1.34	124.3	0.30	0.15	−0.11	−0.14	
1/2–H–top	Cu (Fig. 6b)	−0.73	1.25, 1.26	136.3	0.26	0.12	−0.16	−0.06	
Zn–ad+1/4–H	Cu (Fig. 6a)	−0.84	1.31, 1.30	118.5	0.33	0.12	−0.17	−0.04	−0.04
ZnO–ad+1/2–H–b	Cu (Table S-7e)	−0.66	1.26, 1.34	119.9	0.34	0.11	−0.27	−0.04	−0.00

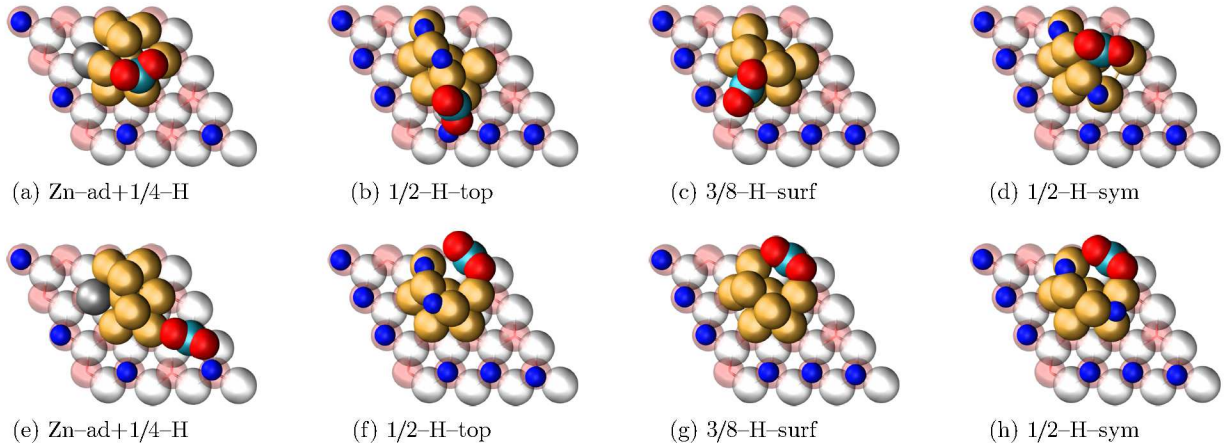

Figure 6. Structure of most stable adsorption sites of CO_2 on four Cu/ZnO catalyst models with each showing Cu cluster and ZnO surface site, see subfigures (a)-(d) and (e)-(h), respectively. Note that all these structures have been fully optimized within our slab model. For the full list of all calculated CO_2 adsorption sites see Table S-3 to Table S-7 of the Supplemental Material. The nomenclature and color code is the same as that used in Fig. 4. In addition, C atoms are shown in light blue.

an electronic structure viewpoint.[118,119] The occupation of the anti–bonding π^* orbital will favor a bent configuration of the surface-adsorbed state of the molecule, i. e., a negatively charged $O-C^{\delta}-O$ species.[118,119]

1. *Exploration of CO_2 adsorption sites*

In a first survey of our Cu/ZnO surface models, we investigated CO_2 adsorption over several high symmetry sites on the ZnO surface. In addition to several possible adsorption modes of our probe molecule on the oxide itself, there exists a large set of adsorption sites and orientations of CO_2 on the metal cluster despite the fact that it consists of a relatively small number of Cu atoms. Thus, an extremely large space of reactant configurations opens up which needs to be examined in order to locate the relevant interaction sites on the catalyst surface. Therefore, we set up a stepwise scheme to explore the PES of adsorption of CO_2 effectively (The work flow is described in the computational methods section as well as in section 2 and section 3 of the Supplementary Material).

Following the results of our surface phase diagram (see Fig. 2) we explored the potential

energy landscape of adsorption of CO_2 for the 1/2–H and 3/8–H phases which are relevant to the conditions of methanol synthesis.[88] In addition, the Zn–ad+1/4–H phase was included which models the enrichment of Zn atoms in the Cu cluster[88] which, earlier, had been observed experimentally[32] and was proposed as active sites only recently[19]. In stark contrast, most recent *in situ* neutron diffraction experiments showed the activation of such migration process to take place only at significantly higher temperatures than those applied in the industrial process of methanol synthesis.[35] Yet, this phenomenon might be relevant to the catalyst preparation procedure. In particular, we have performed a very extensive exploration of the PES for the 1/2–H–sym, 3/8–H–surf, and Zn–ad+1/4–H surface structures. After having obtained stable adsorption sites, which include both parts, i.e. metal cluster and oxide surface, we probed the stability of CO_2 for two more catalyst structures, i. e., the 1/2–H–top and ZnO–ad+1/2–H–b models, but using a less elaborate approach (see computational methods section). Belonging both to the 1/2–H phase, these two structures were considered because 1/2–H–top was identified as the thermodynamic minimum of this phase and ZnO–ad+1/2–H–b addresses another aspect of SMSI, namely the overgrowing of support material onto the Cu cluster.[19]

The local minima resulting from the exploration of CO_2 adsorption sites are summarized in Table I which groups these most stable sites with respect to the two materials, i. e., Cu nanoparticle and ZnO substrate. These two binding modes feature a variety of adsorption sites involving Cu atoms of the cluster and unsaturated O atoms of the ZnO support surface, respectively, in addition to the formation of hydrogen bonds between CO_2 and OH groups of the surface (see structures in Fig. 6). The adsorption strength of CO_2 on the substrate is rather independent on the oxidation state of the support. In contrast, the activity of the nanocatalysts strongly depends on the adsorption site, i. e., Cu cluster or ZnO, which we communicated only very recently for a limited subset of Cu/ZnO surface structures.[88] In the following we will extend our insights into the redox process of CO_2 activation which, besides structural and energetic stability, is determined by the different electronic properties and charge transfer mechanisms of metal nanoparticle and oxide substrate in response to the thermodynamic temperature and (partial) pressure conditions of the gas phase.

2. CO_2 activation on Cu/ZnO

a. Structure and thermodynamic stability. The preferred adsorption structure of CO_2 on the ZnO support is a carbonate-like arrangement[120] for all five nanocatalyst structures. Corresponding values of $E_{\mathrm{ads}}^{\mathrm{CO_2}}$ range from $-0.82\,\mathrm{eV}$ to $-1.09\,\mathrm{eV}$ with a slight preference of Zn–ad+1/4–H and ZnO–ad+1/2–H–b (see Table I). The $E_{\mathrm{ads}}^{\mathrm{CO_2}}$ values of CO_2 at 1/2–H–sym are slightly increased with respect to calculations using the Γ point approximation[88]. Along with similar adsorption energies, comparable structures have been characterized earlier on *bare* ZnO surfaces.[120–124] Nonetheless, here we find that the interaction with the nanoparticle enhances the binding energy at the proximity of the Cu/ZnO interface (see Fig. 6g and Fig. 6h) or obtain substitutional stabilization via hydrogen bonds to OH groups (see Fig. 6e, Fig. 6f, and Table S-7t).

On the Cu cluster, CO_2 adopts a bent adsorption structure which is similar to a CO_2^- species and is found to be similar for all surface structures, i. e., independent of both the particular catalyst model and adsorption site on Cu (see Table I). The values of the adsorption energies $E_{\mathrm{ads}}^{\mathrm{CO_2}}$ range from $-0.66\,\mathrm{eV}$ to -1.41,eV, which is substantially stronger compared to single-crystal ZnO and Cu surfaces as well as unsupported Cu clusters.[120,121,123,125–136] Irrespective of the adsorption site and the catalyst model we obtain a bent configuration of CO_2 with the C−O double bonds being significantly weakened with lengths ranging from 1.23 Å to 1.34 Å (see Fig. 6 and Table I). These values are much larger than the 1.18 Å which we calculated for the isolated CO_2 molecule in the gas phase and therefore indicate an activation of the adsorbed species. The variation in the values of these bond lengths correlates with the increasing coordination number of the O atom of CO_2 and atoms of the Cu cluster, i. e., causing C−O bond elongation which, however, is less pronounced in the carbonate-like species (see Table I). Other than for the carbonate-like adsorption state on the ZnO$(000\bar{1})$ substrate the direct bonding of CO_2 to Zn–ad or ZnO–ad adspecies is thermodynamically not preferred. Over ZnO-ad we could only identify shallow van der Waals-like minima of linear CO_2 species (see Table S-7b on the Supplemental Material).

The by far thermodynamically most stable adsorption site of CO_2 has been found on the Cu cluster of 1/2–H–sym with $E_{\mathrm{ads}}^{\mathrm{CO_2}}$ as low as $-1.41\,\mathrm{eV}$ (see Fig. 6d). This particularly stable adsorbate structure has been discovered when using dynamical AIMD simulations that originally have been conceived to just double-check the stability of 1/2–H–sym-b (see Table I).

The main difference between the two adsorbate structures is the structural distortion of the Cu cluster upon CO_2 adsorption, which leads to higher stability of the adsorbate. This flexibility is immanent to the Cu clusters as such, thus allowing for loosening and formation of new Cu−Cu bonds, which is revealed when using AIMD of the CO_2 adsorbate surface structures. Despite using elevated temperatures of up to 800 K in order to accelerate AIMD exploration of configuration space, this pronounced flexibility clearly points to a rather flat PES that underlies these adsorbate/nanocatalyst complexes. Besides the CO_2 activation over 1/2–H–sym, the same process is largely enhanced on Zn–ad+1/4–H as a result of the flexible nature of the Cu cluster (see Fig. 6a). Although the lowest $E_{\mathrm{ads}}^{\mathrm{CO_2}}$ of CO_2 on Zn-ad+1/4-H is by about 0.6 eV less stable than the global minimum 1/2–H–sym, the structural distortion of the metal cluster of Zn–ad+1/4–H accounts for roughly 0.2 eV of additional stabilization (see Table S-8 in the Supplemental Material). These limited insights already underscore the importance of dynamical effects which cannot be neglected at the outset when studying such processes at elevated temperatures. In particular, at the elevated temperatures of the industrial process, such fluctuation effects contribute to the activation of our putative CO_2 reactant structures despite the fact that they seem to be relatively tightly bound to Cu/ZnO according to their $E_{\mathrm{ads}}^{\mathrm{CO_2}}$ values corresponding to 0 K. In order to explore the high structural flexibility of the CO_2 species on the 1/2–H–sym surface model we have carried out preliminary AIMD simulations ($T = 500$ K) using metadynamics acceleration.[137] In these short simulations multiple adsorption modes were explored in addition to adsorption and desorption processes which were sampled on all parts over Cu/ZnO. Besides such important dynamical effects, we suspect the lattice mismatch of Cu and ZnO causing micro-structural strain at the Cu/ZnO interface[27,36,47] to be the main driving force that enhances CO_2 activation over 1/2–H–sym. In addition to these structural and dynamical insights into the nature of the supported Cu nanoparticle, our calculations reveal that the Cu cluster enhances CO_2 activation much more effectively than the ZnO support itself. This becomes even more evident when analyzing the electronic charge transfer via the Cu/ZnO interface which we will address in the following.

b. Electronic charge transfer. The changes in electronic population of the C and O atoms of CO_2 upon adsorption, i. e., $\Delta q_{\mathrm{CO_2}}(\mathrm{C})$ and $\Delta q_{\mathrm{CO_2}}(\mathrm{O})$, respectively, are summarized in Table I. First of all, there exists a net transfer of electrons to CO_2 of about $0.5\,|e^-|$ for all catalyst structures listed. This strong activation of the probe molecule is a particular

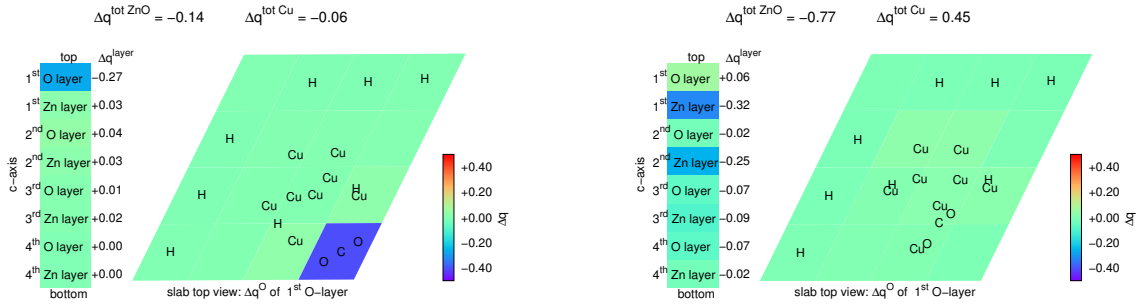

(a) CO_2@O REF: 1/2–H–sym (b) CO_2@Cu REF: 1/2–H–sym

Figure 7. CO_2 activation on the ZnO support (a) and the Cu nanoparticle (b). The difference of the electron population of the individual O and Zn atoms of the 1/2–H–sym nanocatalyst surface structure with and without CO_2 is shown for the local adsorption minima of CO_2 on the support (a) and the metal cluster (b). Further details are analogous to the presentation in Fig. 5.

property of the combined Cu/ZnO system under H-rich conditions. In comparison, almost no CO_2 activation by electronic charge transfer was found for ideal low-index polar ZnO surfaces.[136] Nonetheless, depending on the actual adsorption site, i.e. on the Cu cluster or on the ZnO surface, for our systems this excess charge may localize mainly on the C atom or on the O atoms, respectively. On ZnO, the charge distribution within CO_2 is very similar to that of an isolated carbonate species. Upon adsorption, both metal cluster and ZnO support, become oxidized as shown in Table I by negative values of Δq_{Cu} and Δq_{ZnO}, respectively. Interestingly, for all surfaces forming the carbonate-like species it is the O atom of the ZnO which is mainly oxidized, i. e., adopting almost the same electronic population as the other two O atoms of the adsorbate (see Fig. 7a for 1/2–H–sym and Fig. S4 for all local minima adsorbate structures in the Supplemental Material).

In stark contrast, $O{-}C^{\delta-}{-}O$ species on the metal cluster show an inverted distribution of the excess charge. Its major part, about $0.3\,|e^-|$, is being localized on the C atom irrespectively of oxidation state of the different catalyst models (see Table I). This reduction process involves an orbital which is mainly localized at the C atom (see Fig. 8a/b), but also intermixes with occupied electronic states of the Cu cluster close to the Fermi energy (see pDOSs shown in Fig. 6a to Fig. 6d).

In contrast to the spatially rather homogeneous charge depletion found for the carbonate-like species, the alternative reduction of CO_2 on the metal cluster largely depends on the local redox state of the nanocatalyst structure. In Table I as well as in the corresponding

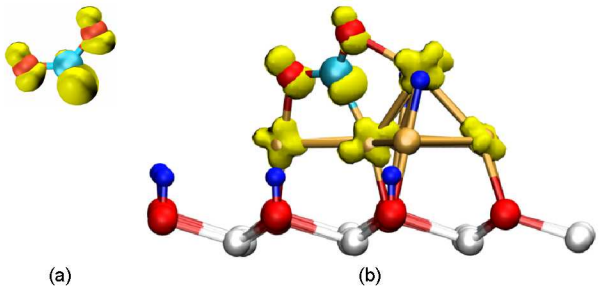

Figure 8. Electronic density plots of (a) the lowest unoccupied molecular orbital (LUMO) of a bent CO_2 molecule in isolation with at fixed OCO angle of 130° and (b) the VB (at the M-point of the BS) of CO_2 being adsorbed on a supported Cu cluster (1/2–H–sym surface structure, see Fig. 6d) resulting in a bent activated structure with an OCO angle of 122.8°. The same color code is used as in Fig. 4 and C atoms are shown in light blue.

spatially resolved electronic charge density difference plot of Fig. 7b (additionally see Fig. S4 in the Supplemental Material) the values of Δq_{Cu} and Δq_{ZnO} indicate oxidation of either metal cluster or oxide substrate. On the one hand, catalyst surface structures like 1/2–H–sym and 1/2–H–sym-b exhibit oxidized Cu clusters but a strongly reduced ZnO substrate (reduced Zn) (compare Fig. 7b and Fig. 5f). This excess electronic charge is transferred to Cu where it initiates the CO_2 reduction process which has been shown in very recent experiments[50]. Yet, positive values of Δq_{Cu} of 1/2–H–sym and 1/2–H–sym-b demonstrate that the reduced Zn of the substrate provides even additional charge that (partially) reduces the Cu cluster as well. On the other hand, the redox process is driven over the Zn–ad+1/4–H surface by a reduced metal cluster alone because of the fully oxidized ZnO substrate. For the in-between case, i.e. if both parts of the catalyst are partially reduced, e. g., in the case of 3/8–H–flat, they must both contribute to achieve full CO_2 activation on Cu. However, the relation of this result to the calculated $E_{\mathrm{ads}}^{\mathrm{CO_2}}$ clearly demonstrates that only excess charge Δq_{Zn} stemming from ZnO (reduced Zn) will result into an enhanced activation of CO_2 on the supported Cu cluster, whereas no further enhancement of this process will take place if the metal is the only the source of reducing charge.

c. Electronic structure. Eventually, the mechanism of charge-transfer-promoted CO_2 activation is made possible by a direct coupling of electronic states close to the Fermi energy. The distinct location of the Fermi energy, however, primarily depends on the oxidation

state of the ZnO substrate which, in turn, is governed by the redox conditions set by the surrounding gas phase as it has been discussed for adsorbate-free catalyst structures (see Fig. 4). Herein, localized Cu states and dispersed bands of ZnO determine the BS of the adsorbate complex surface structures. If very close in energy, these spatially separated bands will mix (compare bands labeled B1 and B2) thus allowing for a direct charge transfer through the Cu/ZnO interface, via O $2p$ and Cu $3d$ orbitals of substrate and cluster, respectively. This electronic-structure-based mechanism of spatial charge redistribution becomes of utmost importance in the activation processes of CO_2 over reduced Cu/ZnO catalyst surfaces especially when the two components, substrate and metal cluster, exhibit different redox states. This is demonstrated by the calculated BSs and pDOSs of CO_2 species being adsorbed on ZnO or Cu clusters (see Fig. S6 and section 6 of the Supplemental Material for a detailed discussion).

IV. SUMMARY, CONCLUSIONS AND OUTLOOK

We carried out comprehensive density functional calculations using thermodynamically optimized slab models in order to disentangle the complex picture of gas phase induced morphological changes of ZnO$(000\bar{1})$-surface-supported copper nanocatalyst systems depending of temperature and pressure conditions of the gas phase. In a second step, these models are used to investigate CO_2 activation on such metal/oxide catalysts.

In-depth analysis of the electronic structure illustrates that even the local redox state of one of the two components, i. e., Cu_8 cluster and ZnO surface, can be tuned by the physical and chemical properties of the gas phase as revealed by the temperature and pressure sensitivity of the structural phase diagram. In the fully oxidized state, a combination of Cu_8 wetting and H adatoms forming hydroxyls is responsible for saturation of more than half of all dangling bonds, while excess of these H species starts to reduce the Zn atoms of the ZnO surface. Because both components are coupled through the Cu/ZnO interface this excess charge can be transferred to the Cu cluster. Cu-Cu cohesion, Zn adatoms, overgrown ZnO addimer, and H adatoms of Cu_8 results only in small modulations of the final surface morphology, while the local redox state rather depends on the chemical nature of the adspecies. Independent of other co-adsorbates, H atoms maintain their charge neutral nature, i. e., the H^0 state, when saturating dangling bonds on the Cu surface and, therefore,

should represent an excellent source of hydrogen for methanol synthesis. Slightly more reduced Cu particles are formed under highly reducing oxygen-poor conditions of the gas phase when strong metal-support interaction sets in. Adopting a similar ionic character as Zn in bulk ZnO, Zn adspecies form at the Cu/ZnO interface of the metal cluster. In the presence of stoichiometric parts of the support material, charge accumulation within the Cu particle is found to be largely canceled and the whole metal cluster will be more oxidized, whereas the ZnO adspecies adopt an ionic character similar to bulk ZnO. According to our phase diagram, the latter surface morphology, resulting from strong metal-support interactions, is thermodynamically disfavored.

Given the complex morphology and redox state "landscape" of the nanocatalyst, a myriad of possible active sites is to be expected. A first glimpse into these active sites has been obtained using a hierarchical exploration scheme based on five selected Cu/ZnO surfaces structures of technological importance. Interestingly, different classes of activated adsorption of CO_2 are found, giving rise to bent $O{-}C^{\delta-}{-}O$ and carbonate-like species on the metal clusters and oxide support, respectively, with binding energies being predominantly independent of their oxidation state. Nonetheless, our results point to an increased reactivity toward CO_2 activation of the Cu nanocatalyst in the presence of reduced Zn in the ZnO substrate. The previously proposed role of reduced Zn atoms on the Cu surface being the active sites is not confirmed by our investigation. Importantly, employing *ab initio* molecular dynamics simulations reveals a surprisingly dynamical nature of the metal nanoparticle at the elevated temperatures relevant to the industrial catalysis process. This generates Cu morphologies that reflect epitaxial strain at the Cu/ZnO interface, which at the temperature and pressure conditions of industrial methanol synthesis leads to an enhanced structural and electronic activation of CO_2 over Cu_8.

Even with this rather small nanocatalyst model we were able to characterize many of the experimental findings of chemical and electronic strong metal-support interaction. Having obtained thermodynamically optimized catalyst structures, i. e., H rich, reduced 1/2–H phase with a large Cu area and atomic H atoms present on the metal, we have the crucial prerequisites at hand to finally start solving the even more complex puzzle of methanol generation from syngas over nanodispersed Cu on ZnO at working conditions of the industrial process. Herein, the presence of complex electronic charge transfer processes over metal/support interface governed by dynamical and morphological changes will open up an enormous space

of chemical and structural configurations, both of adsorbates and catalyst surface, which ultimately is determined by the redox conditions of the surrounding gas phase. Considering all these parameters suggests one to use dynamical sampling approaches in future investigations of metal/oxide catalysts, rather than performing static optimizations of a large set of individual structures as done here. Along this line of thought, we recently developed an efficient computational protocol for computational heterogeneous catalysis based on molecular dynamics. Using this approach, we already studied methanol synthesis from CO over bare ZnO with F–centers using *ab initio* molecular dynamics subject to suitable sampling acceleration in order to compute high-dimensional free energy landscapes. In particular, these finite-temperature simulations resolved the complete reaction network, produced all relevant molecular species, and provided important free energy reaction pathways on bare ZnO. We are currently investigating CO_2 reduction to methanol on Cu/ZnO nanocatalyst models such as those discussed here, again using *ab initio* metadynamics sampling. Interestingly, not only the formation of CO via different mechanisms of the reverse water-gas shift reaction is observed in these simulations, but also side reactions including the production of CH_n species with n from zero up to three. This will significantly enlarge the complexity of the reaction network on the metal/oxide catalyst compared to the one determined previously on bare zinc oxide.

ACKNOWLEDGMENTS

We wish to thank Bernd Meyer for many fruitful discussions. The work is supported by the Cluster of Excellence RESOLV (EXC1069) funded by Deutsche Forschungsgemeinschaft. Computational resources were provided by SuperMUC (München) and BOVILAB@RUB (Bochum).

---

* johannes.frenzel@theochem.rub.de

[1] J. M. Thomas and W. J. Thomas, *Principles and Practice of Heterogeneous Catalysis*, Wiley-VCH, 1996.

[2] K. W. Kolasinski, *Surface Science: Foundations of Catalysis and Nanoscience*, Wiley, 2008.

[3] C. Campbell, A. Grant, D. Starr, S. Parker and V. Bondzie, *Top. Catal.*, 2000, **14**, 43–51.

[4] C. Burda, X. Chen, R. Narayanan and M. A. El-Sayed, *Chem. Rev.*, 2005, **105**, 1025–1102.

[5] P. Sautet and F. Cinquini, *ChemCatChem*, 2010, **2**, 636–639.

[6] S. Schauermann, N. Nilius, S. Shaikhutdinov and H.-J. Freund, *Acc. Chem. Res.*, 2013, **46**, 1673–1681.

[7] S. D. Senanayake, D. Stacchiola and J. A. Rodriguez, *Acc. Chem. Res.*, 2013, **46**, 1702–1711.

[8] C. T. Campbell, *Acc. Chem. Res.*, 2013, **46**, 1712–1719.

[9] K. Foger, *Catalysis: Science and Technology*, Springer-Verlag, 1984.

[10] S. J. Tauster, S. C. Fung and R. L. Garten, *J. Am. Chem. Soc.*, 1978, **100**, 170–175.

[11] K. Waugh, *Catal. Lett.*, 2012, **142**, 1153–1166.

[12] G. A. Olah, *Angew. Chem. Int. Ed.*, 2005, **44**, 2636–2639.

[13] G. A. Olah, A. Goeppert and G. K. Surya Prakash, *Beyond Oil and Gas: The Methanol Economy*, Wiley-VCH, Weinheim, Germany, 2006.

[14] P. Davies, F. F. Snowdon, G. Bridger, D. O. Hughes and P. W. Young, *UK Patent No. 1010871*, 1965.

[15] Y. B. Kagan, L. G. Liberov, E. V. Slivinsky, S. M. Lockev, G. I. Lin, A. Y. Rozovsky and A. N. Bashkirov, *Dokl. Acad. Nauk. SSSR*, 1975, **221**, 1093–1095.

[16] M. Muhler, E. Tørnqvist, L. P. Nielsen, B. S. Clausen and H. Topsøe, *Catal. Lett.*, 1994, **25**, 1–10.

[17] I. Chorkendorff and J. W. Niemantsverdriet, *Concepts of Modern Catalysis and Kinetics*, Wiley-VCH, 2007.

[18] I. Kasatkin, P. Kurr, B. Kniep, A. Trunschke and R. Schlögl, *Angew. Chem. Int. Ed.*, 2007, **46**, 7324–7327.

[19] M. Behrens, F. Studt, I. Kasatkin, S. Kühl, M. Hävecker, F. Abild-Pedersen, S. Zander, F. Girgsdies, P. Kurr, B.-L. Kniep, M. Tovar, R. W. Fischer, J. K. Nørskov and R. Schlögl, *Science*, 2012, **336**, 893–897.

[20] Y. Kanai, T. Watanabe, T. Fujitani, T. Uchijima and J. Nakamura, *Catal. Lett.*, 1996, **38**, 157–163.

[21] M. Spencer, *Catal. Lett.*, 1999, **60**, 45–49.

[22] F. Liao, Y. Huang, J. Ge, W. Zheng, K. Tedsree, P. Collier, X. Hong and S. C. Tsang, *Angew. Chem. Int. Ed.*, 2011, **50**, 2162–2165.

[23] O. Martin and J. Perez-Ramirez, *Catal. Sci. Technol.*, 2013, **3**, 3343–3352.

[24] J. Yoshihara and C. T. Campbell, *J. Catal.*, 1996, **161**, 776–782.

[25] I. Nakamura, T. Fujitani, T. Uchijima and J. Nakamura, *J. Vac. Sci. Technol. A*, 1996, **14**, 1464–1468.

[26] R. Naumann d'Alnoncourt, X. Xia, J. Strunk, E. Löffler, O. Hinrichsen and M. Muhler, *Phys. Chem. Chem. Phys.*, 2006, **8**, 1525–1538.

[27] M. Kurtz, N. Bauer, C. Buescher, H. Wilmer, O. Hinrichsen, R. Becker, S. Rabe, K. Merz, M. Driess, R. A. Fischer and M. Muhler, *Catal. Lett.*, 2004, **92**, 49–52.

[28] M. Kurtz, J. Strunk, O. Hinrichsen, M. Muhler, K. Fink, B. Meyer and C. Wöll, *Angew. Chem. Int. Ed.*, 2005, **44**, 2790–2794.

[29] R. Hadden, B. Sakakini, J. Tabatabaei and K. Waugh, *Catal. Lett.*, 1997, **44**, 145–151.

[30] N.-Y. Topsøe and H. Topsøe, *Top. Catal.*, 1999, **8**, 267–270.

[31] H. Wilmer and O. Hinrichsen, *Catal. Lett.*, 2002, **82**, 117–122.

[32] B. S. Clausen, J. Schiøtz, L. Gråbæk, C. V. Ovesen, K. W. Jacobsen, J. K. Nørskov and H. Topsøe, *Top. Catal.*, 1994, **1**, 367–376.

[33] J. D. Grunwaldt, A. M. Molenbroek, N. Y. Topsøe, H. Topsøe and B. S. Clausen, *J. Catal.*, 2000, **194**, 452–460.

[34] P. L. Hansen, J. B. Wagner, S. Helveg, J. R. Rostrup-Nielsen, B. S. Clausen and H. Topsøe, *Science*, 2002, **295**, 2053–2055.

[35] T. Kandemir, F. Girgsdies, T. C. Hansen, K.-D. Liss, I. Kasatkin, E. L. Kunkes, G. Wowsnick, N. Jacobsen, R. Schlögl and M. Behrens, *Angew. Chem. Int. Ed.*, 2013, **52**, 5166–5170.

[36] M. Günter, T. Ressler, B. Bems, C. Büscher, T. Genger, O. Hinrichsen, M. Muhler and R. Schlögl, *Catal. Lett.*, 2001, **71**, 37–44.

[37] J. J. Liu, *ChemCatChem*, 2011, **3**, 934–948.

[38] M. B. Fichtl, J. Schumann, I. Kasatkin, N. Jacobsen, M. Behrens, R. Schlögl, M. Muhler and O. Hinrichsen, *Angew. Chem. Int. Ed.*, 2014, **53**, 7043–7047.

[39] A. García-Trenco and A. Martínez, *Catal. Today*, 2013, **215**, 152–161.

[40] J. Nakamura, Y. Choi and T. Fujitani, *Top. Catal.*, 2003, **22**, 277–285.

[41] T. Fujitani and J. Nakamura, *Catal. Lett.*, 1998, **56**, 119–124.

[42] S. Kuld, C. Conradsen, P. G. Moses, I. Chorkendorff and J. Sehested, *Angew. Chem. Int. Ed.*, 2014, **53**, 5941–5945.

[43] M. Spencer, *Catal. Lett.*, 1998, **50**, 37–40.

[44] R. Burch, S. E. Golunski and M. S. Spencer, *J. Chem. Soc., Faraday Trans.*, 1990, **86**, 2683–2691.

[45] S. Zander, E. L. Kunkes, M. E. Schuster, J. Schumann, G. Weinberg, D. Teschner, N. Jacobsen, R. Schlögl and M. Behrens, *Angew. Chem. Int. Ed.*, 2013, **52**, 6536–6540.

[46] Y. Kanai, T. Watanabe, T. Fujitani, M. Saito, J. Nakamura and T. Uchijima, *Catal. Lett.*, 1994, **27**, 67–78.

[47] J. B. Wagner, P. L. Hansen, A. M. Molenbroek, H. Topsøe, B. S. Clausen and S. Helveg, *J. Phys. Chem. B*, 2003, **107**, 7753–7758.

[48] S. Natesakhawat, J. W. Lekse, J. P. Baltrus, P. R. Ohodnicki, B. H. Howard, X. Deng and C. Matranga, *ACS Catalysis*, 2012, **2**, 1667–1676.

[49] J. C. Frost, *Nature*, 1988, **334**, 577–580.

[50] F. Liao, Z. Zeng, C. Eley, Q. Lu, X. Hong and S. C. Tsang, *Angew. Chem. Int. Ed.*, 2012, **51**, 5832–5836.

[51] J. Strunk, K. Kähler, X. Xia and M. Muhler, *Surf. Sci.*, 2009, **603**, 1776–1783.

[52] A. J. Medford, J. Sehested, J. Rossmeisl, I. Chorkendorff, F. Studt, J. K. Nørskov and P. G. Moses, *J. Catal.*, 2014, **309**, 397 – 407.

[53] P. W. Tasker, *J. Phys. C: Solid State*, 1979, **12**, 4977–4984.

[54] B. Meyer and D. Marx, *Phys. Rev. B*, 2003, **67**, 035403.

[55] B. Meyer, *Phys. Rev. B*, 2004, **69**, 045416.

[56] G. Kresse, O. Dulub and U. Diebold, *Phys. Rev. B*, 2003, **68**, 245409.

[57] J. V. Lauritsen, S. Porsgaard, M. K. Rasmussen, M. C. R. Jensen, R. Bechstein, K. Meinander, B. S. Clausen, S. Helveg, R. Wahl, G. Kresse and F. Besenbacher, *ACS Nano*, 2011, **5**, 5987–5994.

[58] R. Wahl, J. V. Lauritsen, F. Besenbacher and G. Kresse, *Phys. Rev. B*, 2013, **87**, 085313.

[59] O. Dulub, U. Diebold and G. Kresse, *Phys. Rev. Lett.*, 2003, **90**, 016102.

[60] M. Valtiner, M. Todorova, G. Grundmeier and J. Neugebauer, *Phys. Rev. Lett.*, 2009, **103**, 065502.

[61] M. Valtiner, M. Todorova and J. Neugebauer, *Phys. Rev. B*, 2010, **82**, 165418.

[62] V. Staemmler, K. Fink, B. Meyer, D. Marx, M. Kunat, S. Gil Girol, U. Burghaus and C. Wöll, *Phys. Rev. Lett.*, 2003, **90**, 106102.

[63] B. Meyer and D. Marx, *J. Phys.: Condens. Matter*, 2003, **15**, L89–L94.

[64] S. Shi, C. Shi, K. Fink and V. Staemmler, *Chem. Phys.*, 2003, **287**, 183–195.

[65] B. Meyer, D. Marx, O. Dulub, U. Diebold, M. Kunat, D. Langenberg and C. Wöll, *Angew. Chem. Int. Ed.*, 2004, **43**, 6641–6645.

[66] O. Dulub, B. Meyer and U. Diebold, *Phys. Rev. Lett.*, 2005, **95**, 136101.

[67] M. Kunat, B. Meyer, F. Traeger and C. Wöll, *Phys. Chem. Chem. Phys.*, 2006, **8**, 1499–1504.

[68] Y. Wang, B. Meyer, X. Yin, M. Kunat, D. Langenberg, F. Traeger, A. Birkner and C. Wöll, *Phys. Rev. Lett.*, 2005, **95**, 266104.

[69] R. Kovacik, B. Meyer and D. Marx, *Angew. Chem. Int. Ed.*, 2007, **46**, 4894–4897.

[70] J. Kiss, D. Langenberg, D. Silber, F. Traeger, L. Jin, H. Qiu, Y. Wang, B. Meyer and C. Wöll, *J. Phys. Chem. A*, 2011, **115**, 7180–7188.

[71] H. Qiu, B. Meyer, Y. Wang and Ch. Wöll, *Phys. Rev. Lett.*, 2008, **101**, 236401.

[72] K. Fink, *Phys. Chem. Chem. Phys.*, 2006, **8**, 1482–1489.

[73] G. Rossmueller, V. Kleinschmidt, J. Kossmann and C. Haettig, *J. Phys. Chem. C*, 2009, **113**, 1418–1425.

[74] J. Kossmann, G. Rossmüller and C. Hättig, *J. Chem. Phys.*, 2012, **136**, 034706.

[75] H. Wilmer, M. Kurtz, K. V. Klementiev, O. P. Tkachenko, W. Grunert, O. Hinrichsen, A. Birkner, S. Rabe, K. Merz, M. Driess, C. Wöll and M. Muhler, *Phys. Chem. Chem. Phys.*, 2003, **5**, 4736–4742.

[76] S. Polarz, J. Strunk, V. Ischenko, M. W. E. van den Berg, O. Hinrichsen, M. Muhler and M. Driess, *Angew. Chem. Int. Ed.*, 2006, **45**, 2965–2969.

[77] J. Kiss, A. Witt, B. Meyer and D. Marx, *J. Chem. Phys.*, 2009, **130**, 184706.

[78] J. Kiss, J. Frenzel, B. Meyer and D. Marx, *J. Chem. Phys.*, 2013, **139**, 044705.

[79] J. Kiss, J. Frenzel, N. N. Nair, B. Meyer and D. Marx, *J. Chem. Phys.*, 2011, **134**, 064710.

[80] J. Frenzel, J. Kiss, N. N. Nair, B. Meyer and D. Marx, *Phys. Status Solidi B*, 2013, **250**, 1174–1190.

[81] J. Frenzel and D. Marx, *J. Chem. Phys.*, 2014, **141**, 124710.

[82] B. Meyer and D. Marx, *Phys. Rev. B*, 2004, **69**, 235420.

[83] Y.-T. Cheng, T.-R. Shan, B. Devine, D. Lee, T. Liang, B. B. Hinojosa, S. R. Phillpot, A. Asthagiri and S. B. Sinnott, *Surf. Sci.*, 2012, **606**, 1280 – 1288.

[84] D. B. Rasmussen, T. V. Janssens, B. Temel, T. Bligaard, B. Hinnemann, S. Helveg and J. Sehested, *J. Catal.*, 2012, **293**, 205 – 214.

[85] K. H. Ernst, A. Ludviksson, R. Zhang, J. Yoshihara and C. T. Campbell, *Phys. Rev. B*, 1993, **47**, 13782–13796.

[86] J. Yoshihara, J. Campbell and C. Campbell, *Surf. Sci.*, 1998, **406**, 235–245.

[87] I. Hegemann, A. Schwaebe and K. Fink, *J. Comput. Chem.*, 2008, **29**, 2302–2310.

[88] L. Martínez-Suárez, J. Frenzel, D. Marx and B. Meyer, *Phys. Rev. Lett.*, 2013, **110**, 086108.

[89] B. Yoon, H. Häkkinen, U. Landman, A. S. Wörz, J.-M. Antonietti, S. Abbet, K. Judai and U. Heiz, *Science*, 2005, **307**, 403–407.

[90] E. Wahlström, N. Lopez, R. Schaub, P. Thostrup, A. Rønnau, C. Africh, E. Lægsgaard, J. K. Nørskov and F. Besenbacher, *Phys. Rev. Lett.*, 2003, **90**, 026101.

[91] S. A. French, A. A. Sokol, C. R. A. Catlow and P. Sherwood, *J. Phys. Chem. C*, 2008, **112**, 7420–7430.

[92] M. Behrens, G. Lolli, N. Muratova, I. Kasatkin, M. Hävecker, R. N. d'Alnoncourt, O. Storcheva, K. Köhler, M. Muhler and R. Schlögl, *Phys. Chem. Chem. Phys.*, 2013, **15**, 1374–1381.

[93] K. Tohji, Y. Udagawa, T. Mizushima and A. Ueno, *J. Phys. Chem.*, 1985, **89**, 5671–5676.

[94] C. T. Campbell, K. A. Daube and J. White, *Surf. Sci.*, 1987, **182**, 458 – 476.

[95] R. Zhang, A. Ludviksson and C. Campbell, *J. Catal.*, 1994, **25**, 277–292.

[96] L. Bengtsson, *Phys. Rev. B*, 1999, **59**, 12301–12304.

[97] M. Farnesi Camellone and D. Marx, *J. Phys. Chem. C*, 2014, **118**, 20989–21000.

[98] P. Giannozzi, S. Baroni, N. Bonini, M. Calandra, R. Car, C. Cavazzoni, D. Ceresoli, G. L. Chiarotti, M. Cococcioni, I. Dabo, A. Dal Corso, S. de Gironcoli, S. Fabris, G. Fratesi, R. Gebauer, U. Gerstmann, C. Gougoussis, A. Kokalj, M. Lazzeri, L. Martin-Samos, N. Marzari, F. Mauri, R. Mazzarello, S. Paolini, A. Pasquarello, L. Paulatto, C. Sbraccia, S. Scandolo, G. Sclauzero, A. P. Seitsonen, A. Smogunov, P. Umari and R. M. Wentzcovitch, *J. Phys.–Condens. Mat.*, 2009, **21**, 5502.

[99] J. Hutter *et al.*, *CPMD v3.15*, Copyright IBM Corp 1990-2011, Copyright MPI für Festkörperforschung Stuttgart 1997-2001, `http://www.cpmd.org`.

[100] D. Marx and J. Hutter, *Ab Initio Molecular Dynamics: Basic Theory and Advanced Methods*, Cambridge University Press, Cambridge, 2009.

[101] J. P. Perdew, K. Burke and M. Ernzerhof, *Phys. Rev. Lett.*, 1996, **77**, 3865–3868.J. P. Perdew, K. Burke and M. Ernzerhof, *Phys. Rev. Lett.*, 1997, **78**, 1396.

[102] V. I. Anisimov, J. Zaanen and O. K. Andersen, *Phys. Rev. B*, 1991, **44**, 943–954.

[103] D. Vanderbilt, *Phys. Rev. B*, 1990, **41**, 7892–7895.

[104] H. J. Monkhorst and J. D. Pack, *Phys. Rev. B*, 1976, **13**, 5188–5192.

[105] E. Kaxiras, K. C. Pandey, Y. Bar-Yam and J. D. Joannopoulos, *Phys. Rev. Lett.*, 1986, **56**, 2819–2822.

[106] E. Kaxiras, Y. Bar-Yam, J. D. Joannopoulos and K. C. Pandey, *Phys. Rev. B*, 1987, **35**, 9625–9635.

[107] G.-X. Qian, R. M. Martin and D. J. Chadi, *Phys. Rev. B*, 1988, **38**, 7649–7663.

[108] K. Reuter and M. Scheffler, *Phys. Rev. B*, 2001, **65**, 035406.

[109] B. Meyer, in *Computational Nanoscience: Do It Yourself!*, ed. D. M. J. Grotendorst, S. Blugel, John von Neumann Institute for Computing, Julich, 2006, vol. 31, ch. Surface Phase Diagrams from Ab Initio Thermodynamics, pp. 411–418.

[110] G. J. Martyna, M. L. Klein and M. Tuckerman, *J. Chem. Phys.*, 1992, **97**, 2635–2643.

[111] P.-O. Löwdin, *J. Chem. Phys.*, 1950, **18**, 365–375.

[112] S. Grimme, *J. Comput. Chem.*, 2006, **27**, 1787–1799.

[113] G. Mercurio, E. R. McNellis, I. Martin, S. Hagen, F. Leyssner, S. Soubatch, J. Meyer, M. Wolf, P. Tegeder, F. S. Tautz and K. Reuter, *Phys. Rev. Lett.*, 2010, **104**, 036102.

[114] K. Tonigold and A. Groß, *J. Chem. Phys.*, 2010, **132**, 224701.

[115] U. Ozgur, Y. I. Alivov, C. Liu, A. Teke, M. A. Reshchikov, S. Dogan, V. Avrutin, S.-J. Cho and H. Morkoc, *J. Appl. Phys.*, 2005, **98**, 041301.

[116] Z. Liu, A. Rittermeier, M. Becker, K. Käahler, E. Löffler and M. Muhler, *Langmuir*, 2011, **27**, 4728–4733.

[117] V. Schott, H. Oberhofer, A. Birkner, M. Xu, Y. Wang, M. Muhler, K. Reuter and C. Wöll, *Angew. Chem. Int. Ed.*, 2013, **52**, 11925–11929.

[118] S.-G. Wang, X.-Y. Liao, D.-B. Cao, C.-F. Huo, Y.-W. Li, J. Wang and H. Jiao, *J. Phys. Chem. C*, 2007, **111**, 16934–16940.

[119] H. J. Freund and M. W. Roberts, *Surf. Sci. Rep.*, 1996, **25**, 225–273.

[120] Y. Wang, R. Kováčik, B. Meyer, K. Kotsis, D. Stodt, V. Staemmler, H. Qiu, F. Traeger, D. Langenberg, M. Muhler and C. Wöll, *Angew. Chem. Int. Ed.*, 2007, **46**, 5624–5627.

[121] J. Saussey, J.-C. Lavalley and C. Bovet, *J. Chem. Soc., Faraday Trans. 1*, 1982, **78**, 1457–1463.

[122] T. Shido and Y. Iwasawa, *J. Catal.*, 1993, **140**, 575–584.

[123] Y. Wang, X. Xia, A. Urban, H. Qiu, J. Strunk, B. Meyer, M. Muhler and C. Wöll, *Angew.*

Chem. Int. Ed., 2007, **46**, 7315–7318.

[124] K. Kotsis, D. Stodt, V. Staemmler, R. Kovacik, B. Meyer, F. Traeger, D. Langenberg, T. Strunskus, M. Kunat and C. Wöll, *Z. Phys. Chem.*, 2008, **222**, 891–915.

[125] M. Bowker, H. Houghton and K. C. Waugh, *J. Chem. Soc., Faraday Trans. 1*, 1981, **77**, 3023–3036.

[126] M. Bowker, H. Houghton, K. C. Waugh, T. Giddings and M. Green, *J. Catal.*, 1983, **84**, 252–255.

[127] C. Au, W. Hirsch and W. Hirschwald, *Surf. Sci.*, 1989, **221**, 113 – 130.

[128] C. T. Au and M. D. Chen, *Chem. Phys. Lett.*, 1997, **278**, 238 – 244.

[129] J. Wang, S. Funk and U. Burghaus, *J. Chem. Phys.*, 2005, **123**, 204710.

[130] G. Wang, Y. Morikawa, T. Matsumoto and J. Nakamura, *J. Phys. Chem. B*, 2006, **110**, 9–11.

[131] D. Mei, L. Xu and G. Henkelman, *J. Catal.*, 2008, **258**, 44–51.

[132] Y. Yang, J. Evans, J. A. Rodriguez, M. G. White and P. Liu, *Phys. Chem. Chem. Phys.*, 2010, **12**, 9909–9917.

[133] D. Esken, H. Noei, Y. Wang, C. Wiktor, S. Turner, G. Van Tendeloo and R. A. Fischer, *J. Mater. Chem.*, 2011, **21**, 5907–5915.

[134] H. Noei, C. Wöll, M. Muhler and Y. Wang, *Appl. Catal., A*, 2011, **391**, 31 – 35.

[135] H. Noei, C. Wöll, M. Muhler and Y. Wang, *J. Phys. Chem. C*, 2011, **115**, 908–914.

[136] Q.-L. Tang and Q.-H. Luo, *J. Phys. Chem. C*, 2013, **117**, 22954–22966.

[137] A. Laio and M. Parrinello, *Proc. Natl. Acad. Sci. U. S. A.*, 2002, **99**, 12562–12566.